GMIE-100: A global maximum irrigation extent and irrigation type dataset derived via irrigation performance during drought stress and machine learning methods

Fuyou Tian[1], Bingfang Wu[1,2,*], Hongwei Zeng[1,2], Miao Zhang[1], Weiwei Zhu[1], Nana Yan[1], Yuming Lu[1,2]
Yifan Li [3,1]

[1]State Key Laboratory of Remote Sensing Science, Aerospace Information Research Institute, Chinese Academy of Sciences, Beijing 100101, China;
[2]University of Chinese Academy of Sciences, Beijing 100049, China;
[3]School of Computer Science, China University of Geosciences, Wuhan 430078, China

Correspondence to: Bingfang Wu (wubf@aircas.ac.cn)

Abstract. Irrigation accounts for the major form of human water consumption and plays a pivotal role in enhancing crop yields and mitigating drought effects. The precise distribution of irrigation is crucial for effective water resource management and the assessment of food security. However, the resolution of the global irrigated cropland map is coarse, typically approximately 10 kilometres, and the map is not regularly updated. In our study, we present a robust methodology that leverages irrigation performance during drought stress as an indicator of crop productivity and water consumption to identify global irrigated cropland. Within each irrigation mapping zone (IMZ), we identified the dry months of the growing season from 2017 to 2019 or the driest months from 2010 to 2019. To delineate irrigated cropland, we utilized the collected samples to calculate normalized difference vegetation index (NDVI) thresholds for the dry months of 2017 to 2019 and the NDVI deviation from the ten-year average for the driest month. By combining the most accurate results of these two methods, we generated the Global Maximum Irrigation Extent dataset at 100-metre resolution (GMIE-100), achieving an overall accuracy of 83.6%±0.6%. The GMIE-100 reveals that the maximum extent of irrigated cropland encompasses 403.17±9.82 million hectares, accounting for 23.4% ±0.6% of the global cropland. Concentrated in fertile plains and regions adjacent to major rivers, the largest irrigated cropland areas are found in India, China, the United States, and Pakistan, which rank 1st to 4th, respectively. Importantly, the spatial resolution of GMIE-100 surpasses that of the dominant irrigation map, offering more detailed information essential for supporting estimates of agricultural water use and regional food security assessments. Furthermore, with the help of the deep learning (DL) method, the global central pivot irrigation system (CPIS) was identified using Pivot-Net, a novel convolutional neural network based on U-net. We found that there are 11.5±0.01 million hectares of CPIS, accounting for approximately 2.90%±0.03% of the total irrigated cropland. In Namibia, the US, Saudi Arabia, South Africa, Canada, and Zambia, the CPIS proportion was greater than 10%. To our knowledge, this study is the first attempt to identify irrigation methods globally. The GMIE-100 dataset containing both the irrigated extent and CPIS distribution is accessible on Harvard Dataverse at https://doi.org/10.7910/DVN/HKBAQQ (Tian et al., 2023a).

1. Introduction

Irrigation plays a pivotal role in mitigating the impacts of drought events (Wang et al., 2021; Wu et al., 2022). As climate change has intensified, droughts and heatwaves have become more frequent; thus, irrigation has emerged as an effective strategy to counter these extreme events and bolster the resilience of agricultural systems (Mcdermid et al., 2023). However, irrigation represents a significant human intervention in the global water cycle, as it accounts for 67% of global freshwater withdrawal and 87% of total water consumption (Wu et al., 2022). Therefore, accurate information pertaining to irrigation is important for both crop monitoring and water resource management purposes (Wu et al., 2023b; Tian et al., 2022). However, the highest available resolution for existing irrigation maps remains within a range of 500 metres to 10 kilometres (Nagaraj et al., 2021; Siebert et al., 2005; Siebert et al., 2013). This limitation falls far short of the resolution needed to adequately support crop condition monitoring and sustainable water resource management at the subbasin level (Zhang et al., 2022c; Xie and Lark, 2021).

Traditionally, two methods have been employed for generating gridded irrigation maps. The first method involves the allocation of statistical data that uses specific indicators such as land cover area, peak normalized difference vegetation index (NDVI) values, and irrigation potential indices (Zhu et al., 2014; Pervez and Brown, 2010; Zajac et al., 2022). Notably, the Food and Agriculture Organization (FAO) utilized this approach to produce the Global Map of Irrigation Area (FAO-GMIA) from 1995 to 2005 at a 10-kilometre resolution; this renowned irrigation map is widely applied in global water resource management (Siebert et al., 2015). At the national scale, several irrigation maps for China have been produced with resolutions ranging from 500 to 1000 metres; these maps primarily utilize data from the Chinese Statistical Yearbook (Zhu et al., 2014; Zhang et al., 2022b). For the United States, Pervez and Brown (2010) developed an Irrigated Agriculture Dataset for the US (MIrAD-US) with a resolution of 250 metres. Zajac et al., 2022, produced the European Irrigation Map for 2010 (EIM2010), albeit with a coarser 10-kilometre×10-kilometre resolution. Importantly, the accuracy of irrigated cropland maps generated through these methods relies heavily on the representativeness of the spatial allocation indicators and the precision of the statistical data. The indicators used to allocate irrigation areas to each grid often fail to capture the precise distribution of irrigated cropland, especially in humid regions (Pervez and Brown, 2010). Consequently, achieving higher-resolution irrigation maps via this approach can be challenging. Furthermore, due to variations in terrain types and irrigation techniques, census data may underestimate the actual irrigation area (Zhang et al., 2022c). Furthermore, data from different departments may exhibit discrepancies owing to differing statistical criteria. For example, in 2010, the reported irrigation area in California differed by more than 10% between the US Geological Survey and the state's Department of Water Resources (Meier et al., 2018).

Scholars have sought to independently derive irrigated cropland via spectral signatures (Thenkabail et al., 2009; Salmon et al., 2015). The peak values in time-series vegetation indices can serve as indicators of crop water stress, biomass, and chlorophyll content. Given that irrigated crops typically exhibit reduced water stress and elevated chlorophyll content, disparities in peak vegetation index values can be harnessed to differentiate between irrigated and rainfed croplands.

Commonly employed vegetation indices for this approach include the NDVI, greenness index (GI), land surface water index (LSWI), chlorophyll vegetation index (GCVI), enhanced vegetation index (EVI), and others (Shahriar Pervez et al., 2014; Lu et al., 2021; Chen et al., 2018; Xiang et al., 2019; Dela Torre et al., 2021). The discrimination between irrigated and rainfed croplands is typically accomplished through thresholding or decision tree classification and relies on selected vegetation indices. Nevertheless, importantly, vegetation indices may not entirely capture crop water stress, leading to subtle differences in peak vegetation indices and complicating the mapping of large-scale irrigated farmland.

To enhance the distinction of irrigated cropland, supervised classification models incorporate climate variables and environmental factors such as precipitation, temperature, surface temperature, and terrain (Salmon et al., 2015). For instance, Thenkabail et al. (2009) utilized a set of factors, including AVHRR vegetation index time series, precipitation data, elevation information, and vegetation cover maps, as inputs to a decision tree classifier, resulting in the creation of the first global irrigation area map (IWMI-GIAM) at a 10-kilometre resolution based on remote sensing data. Salmon et al. (2015) employed MODIS vegetation indices and 19 climate variables to produce the Global Rainfed and Irrigated Cropland map (GRIPC-500) for 2005 at a resolution of 500 metres.

In recent years, the mapping of irrigated croplands at the national and regional scales has undergone significant advancements due to the availability of extensive meteorological and remote sensing data stored in Google Earth Engine (GEE) (Zhang et al., 2022c; Deines et al., 2019; Xie et al., 2019; Xie and Lark, 2021). Xie et al. (2021) developed a random forest model incorporating a wide array of variables, including environmental factors (precipitation, Palmer drought severity index, soil moisture, aridity index, land surface and air temperature), vegetation indices (NDVI, NDWI, GCVI, WGI, and AGI), and ground irrigation samples. This model achieved an impressive 30-metre resolution irrigation dataset for the United States (LANID). Subsequently, Zhang et al. (2022a) applied this methodology to generate an irrigated cropland map for China from 2000 to 2019 with a resolution of 500 metres (IrriMap_CN). In the same year, Zhang et al. (2022c) enhanced the resolution of the irrigation cropland distribution map for China to 250 metres. However, this method heavily relies on samples, and the spatial representativeness of these irrigation and rainfed samples directly influences the accuracy of the results (Zhang et al., 2022c). Collecting ground sample points is a labour-intensive and time-consuming process, and ensuring their spatial representativeness across larger areas, including at a global scale, poses considerable challenges (Zhang et al., 2022b; Zhang et al., 2022d; Tian et al., 2022).

Though various irrigation maps exist at global and national scales, many of these maps suffer from either very low spatial resolution or outdated information, as outlined in Table 1 (Dari et al., 2023). While some high-resolution irrigation maps are annually updated, they are typically applicable only at a national level (Zhang et al., 2022c; Xie et al., 2021). In essence, the challenge of generating a higher-resolution and up-to-date global irrigated cropland map via supervised methods persists.

An additional significant issue is the phenomenon of "mixed pixels" in MODIS data, which is particularly pronounced in regions with fragmented croplands, such as farmlands in southern China and Africa, where agricultural fields are often smaller

than one MODIS pixel (0.25 hectares) (Zhang et al., 2022a). Consequently, global irrigation map with higher resolution are urgently needed to support both water resource management and food security assessments.

Inspired by the fundamental purpose of irrigation, which is to alleviate the impact of drought, we introduced the Global Maximum Irrigated Extent with 100-metre resolution (GMIE-100) dataset. This dataset leverages irrigation performance during periods of drought stress. When drought conditions prevail, disparities in crop conditions, as indicated by the peak NDVI values, become more pronounced between irrigated and rainfed farmlands. This amplification enables the precise identification of irrigated farmland across most regions while also reducing the quantity of required training samples (Wu et al., 2023a).

Furthermore, considerable variations in irrigation efficiency are apparent among different irrigation types, with central pivot irrigation systems (CPISs), which have an efficiency rate exceeding 80%, emerging as the predominant global sprinkler irrigation method (Tian et al., 2023b). In contrast, gravity-flowing irrigation methods, while widespread, exhibit a comparatively lower efficiency rate of approximately 60% (Waller and Yitayew, 2016). Despite the important role of irrigation in agriculture, few studies have been dedicated to the remote sensing identification of various irrigation types, indicating a notable gap in scientific exploration. Notably, the unique circular configuration of CPISs facilitates their visual interpretation from satellite imagery, presenting an avenue for enhanced monitoring and analysis through remote sensing technologies. The advent of deep learning (DL) has opened avenues for the classification of irrigation methods based on distinctive spatial patterns, such as CPIS. In this study, Pivot-Net, a shape attention neural network designed for CPIS identification in satellite imagery, was used, and a global CPIS dataset (GCPIS) was generated to estimate the proportion of irrigation methods for CPIS.

Table 1 List of existing irrigation maps at the global or national scale.

Dataset	Coverage	Spatial Resolution	Time	Method summary	Reference
Global Irrigated Area Map (IWMI-GIAM)	Global	10 km	2000,	Uses decision tree classifier with vegetation index &environmental data as input	(Thenkabail et al., 2009)
Global Map of Irrigation Area (FAO-GMIA)	Global	10 km	1995/2000/2005	Allocates census data based on landcover area	(Siebert et al., 2015)
Global Rainfed, Irrigated and Paddy Croplands (GRIPC-500)	Global	500 m	Single map 2005	Includes climate variables and environmental factors in a decision tree classifier	(Salmon et al., 2015)
Global Food-Support Analysis Data (GFSAD)	Global	1 km	2010	Created using multiple input data including satellite data, climatic and census data.	(Thenkabail et al., 2012)
Landsat-derived Global Rainfed and Irrigated-Cropland Product at nominal 30 m of the World (USGS-LGRIP30)	Global	30 m	2015	Landsat-derived global rainfed and irrigated cropland product within cropland extent	(Teluguntla et al., 2023)

Landsat-based Irrigation Dataset (LANID)	US	30 m	1997-2017	Random forest model based on environmental variables & vegetation indices (Xie et al., 2021; Xie et al., 2019; Xie and Lark, 2021)
Annual irrigation maps across China (IrriMap_CN)	China	500 m	2000-2019	Random forest with remote sensing index and environmental index (Zhang et al., 2022c)
Remotely sensed high resolution irrigated area in India	India	250 m	2000-2015	NDVI series in decision tree method (Ambika et al., 2016)

2. Materials and methods

Taking inspiration from the fundamental purpose of irrigation, our aim is to identify periods of drought stress to accentuate the disparities in crop conditions between irrigated and rainfed croplands. We initiated this process by utilizing the sixty-five monitoring and reporting units (MRUs) established by CropWatch (Wu et al., 2015; Gommes et al., 2016). These MRUs, which consider factors such as crop types, agricultural potential, and environmental conditions, served as the basis for further dividing global cropland into 110 irrigation mapping zones (IMZs). The first-level 65 agroecological zones offer a fundamental global overview. To address limitations in depicting water stress and irrigation within zones, a more detailed classification was introduced, creating second-level agroecological zones based on arid indices, water availability, soil types, and landforms. Ultimately, we utilized 110 IMZs as the foundational units for determining the specific timing of drought stress, as illustrated in

Figure 1. This comprehensive approach allowed us to capture and amplify the distinctions in crop conditions between irrigated and rainfed croplands.

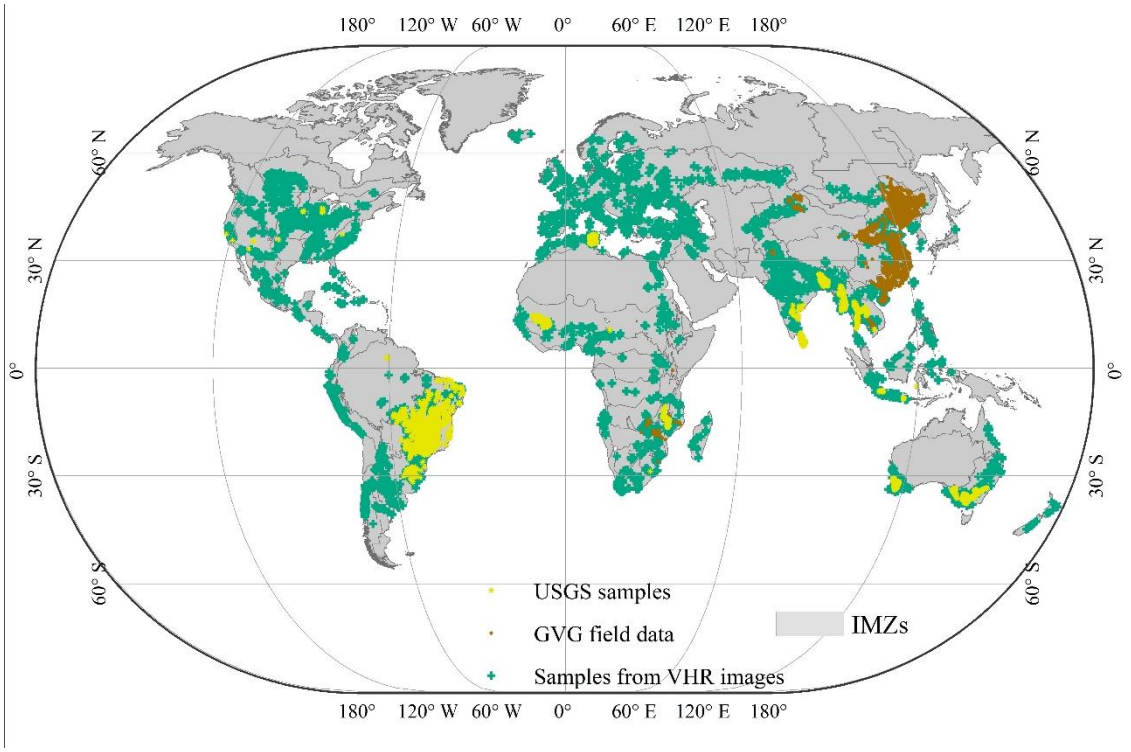

Figure 1 Samples of irrigated, rainfed and central pivot irrigation system (CPIS) from multiple sources and mapping units for irrigation mapping and CPIS identification. GVG means GPS, Video, GIS system for collecting field data. VHR means very high resolution. IMZs means Irrigation mapping zones.

The general framework for detecting drought stress and evaluating crop conditions in irrigated and rainfed cropland is illustrated in Figure 2. Inspired from purpose of irrigation, what is to mitigate the effect of water stress. Basically, we assume that water stress can be regular or irregular. If there are crops during dry season, the irrigation should occur regular. Otherwise, irrigation is just complementary to rainfall in extremely dry year, which means irrigation is irregular. For regular irrigation, we could detect vegetation signal in the dry season (DM-NDVI) when precipitation couldn't meet water demand for crops. For irregular irrigation, we compare the NDVI in extremely dry year with 10-year average level and calculate the deviation ($NDVI_{dev}$) to determine whether it is irrigated or not. To determine whether, it is region with regular or irregular irrigation, we used both of these two indicators and choose the method get higher accuracy.

Then, with the support of the DL model, a CPIS identification model focused on circular shapes was trained and applied to the entire world to generate global CPIS distribution data. The extent of the CPIS was recognized as the extent of irrigation used to update the global extent of irrigation. Finally, we estimated the proportion of irrigation types in the CPIS within irrigated cropland.

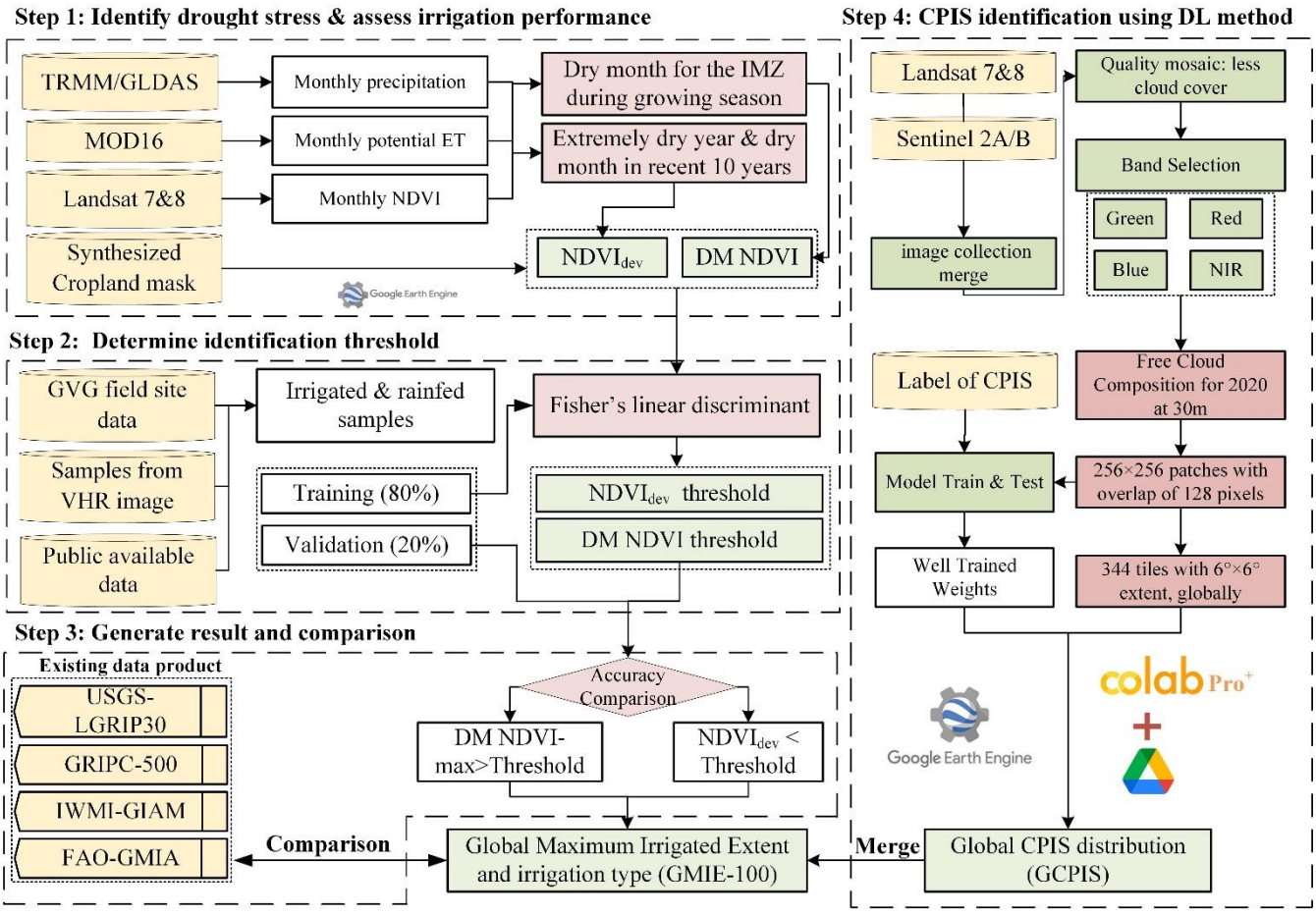

Figure 2 Flow chart of GMIE-100 with a typical irrigation type of CPIS. GVG means GPS, Video, GIS system for collecting field data. VHR means very high resolution. IMZs means Irrigation mapping zones. $NDVI_{dev}$: NDVI deviation in extremely dry year with 10-year average level. DM-NDVI: NDVI in the dry season.

2.1 Input data

In this research, the distribution of rainfall on a global scale plays a pivotal role in determining the necessity for crop irrigation. The focus of this study was the ten-year period from 2010 to 2019 and the aim was to identify the driest year within this timeframe. Two distinct sources of precipitation data were utilized: a) tropical rainfall measuring mission (TRMM) data from the TRMM collection TRMM/3B43V7, which provides monthly precipitation estimates, was employed for geographical areas ranging from 50°S to 50°N. This data source offers insights into precipitation patterns within this specific region; b) global land data assimilation system (GLDAS) data for precipitation was used for areas outside the 50°S to 50°N range, as GLDAS provides information on precipitation in regions beyond the tropical band.

Additionally, the evapotranspiration product, MOD16A2.006, which was introduced by Mu et al. in 2013, was utilized. This product can determine the water surplus during the driest months within each IMZ. The MOD16A2.006 dataset is characterized by an 8-day composite timeframe and a pixel resolution of 500 metres. It is derived from the Penman–Monteith equation and incorporates both daily meteorological reanalysis data and remotely sensed data products from MODIS. This comprehensive dataset aids in the assessment of water availability and evapotranspiration dynamics during critical dry periods.

The 30-metre spatial resolution NDVI data from the Landsat sensors Thematic Mapper (TM), Enhanced Thematic Mapper Plus (ETM+), and Thermal Infrared Sensor (OLI-TIRS) onboard Landsat-5, Landsat-7, and Landsat-8, respectively, were utilized in Google Earth Engine (GEE) (Gorelick et al., 2017) to differentiate irrigated and nonirrigated areas across various IMZs during a specific period. The NDVI data was masked using the cloud and water mask in the flag file and rescaled into the same range between -1 and 1.

2.2 Sample Data

Acquiring irrigation samples on a global scale presents an enormous challenge that is characterized by significant labour and cost requirements, primarily attributable to the extensive geographic scope. To globally classify irrigated and nonirrigated cropland, a single dataset of adequately representative samples is needed; however, such a dataset does not currently exist. The scarcity of irrigation datasets tailored to specific crop types hinders precise differentiations between irrigated and nonirrigated croplands. In most countries, except for India, China, and Pakistan, the area allocated to irrigated croplands constitutes a relatively minor fraction of the total cultivated area. This paucity of representation poses challenges in amassing a substantial sample size suitable for classification purposes. Contemporary irrigation maps often have coarse spatial resolutions, which curtail their efficacy in generating precise samples for classification endeavours. To overcome these limitations and establish a robust sample dataset, an integrative methodology was employed. This approach entailed the fusion of data originating from three independent sources, facilitating a more comprehensive and accurate appraisal of global irrigated and nonirrigated croplands.

The first source involves field data points collected using the GVG (GPS, Video, GIS) application in China (surveyed from 2010 to 2019), Cambodia (in 2019), Ethiopia (from 2018 to 2019), Zambia (from 2016 to 2019), Mozambique (from 2016 to 2019), and Zimbabwe (from 2016 to 2019). This application serves as a comprehensive field data collection system that integrates GPS for precise positioning, a video for capturing geo-tagged photographs, and a GIS system for managing geographic information (Wu et al., 2023a; Wu et al., 2020), which can be download via https://gvgserver.cropwatch.com.cn/download. By conducting observations of irrigation infrastructure, including irrigation canals, reservoirs, lakes, rivers, and irrigation wells, and through interactions with farmers, we were able to determine the types of irrigation in the fields. Also, irrigated was applied for certain crop types, such as winter wheat in North China Plain, Cotton in Xinjiang and vegetable and tomatoes in most province, et.al. Meanwhile, irrigated crops usually appear greener and lush compared with near crops. Even it cannot be distinguished following above characteristics, the injury of local farmer could

give the answer. The collected dataset comprises a total of 78,338 sample points, including 36,809 rainfed samples and 41,529 irrigation samples, with the majority of these points located in China, totalling 72,224 points.

The second data source consists of validation points collected as part of the Global Food Security Analysis Data 30 (GFSAD30) project, which is made available to the public through the website https://croplands.org/app/data/search. This project is a collaborative effort involving the United States Geological Survey (USGS), various universities, research institutions, and companies such as Google. These sample points were collected or derived as part of the project's objective to support global food security analysis at a 30-metre spatial resolution. Some of the sample points were gathered through field surveys conducted using mobile applications. Others were derived by interpreting remote sensing imagery, such as MODIS and Landsat TM data, crop-specific thematic maps, foundational geographic data (e.g., road networks), and other geospatial information (e.g., elevation data layers). The dataset encompasses a total of 17,076 sample points, comprising 3,000 rainfed points and 14,076 irrigated points. The majority of these points are located in Brazil (13,368), Australia (2,192), Thailand (393), and Tunisia (389).

The third supplementary data source involved the acquisition of samples through visual interpretation of very high-resolution (VHR) images available in GEE. The following irrigation points were selected based on identifiable irrigation infrastructure: 1) central pivot irrigation systems, which are easy to identify due to their shapes; 2) clearly visible irrigation systems, which are clearly visible on VHR images; 3) rain-deficient cultivated areas, which are areas classified as cropland with insufficient rainfall but exhibiting NDVI values indicating vegetation presence and annual growth rings; and 4) high vegetation signals during dry seasons, which are areas displaying elevated vegetation signals during dry seasons. The United Nations Food and Agriculture Organization's Global Map of Irrigation Areas (FAO GMIA) (Siebert et al., 2013) and the World Heritage Irrigation Structures (WHIS) list (https://www.icid.org/icid_his1.php#HIS) were used as reference sources. The FAO GMIA's Irrigation Areas of Interest (AEI) and WHIS listings were consulted to identify irrigation areas. Rainfed irrigation points were selected based on FAO GMIA's criteria. If a region lacked any irrigation infrastructure and the AEI value from the FAO GMIA was zero, the area was classified as a rainfed irrigation sample.

Figure 1 illustrates a total of 115,379 sample points. Eighty percent of this dataset, or 92,303 points (comprising 37,650 rainfed and 54,653 irrigated points), was employed for training or calibrating the threshold. The remaining 20%, or 23,076 points (comprising 10,892 rainfed cropland points and 12,184 irrigated points), were used for result validation.

2.3 Land cover and cropland datasets

In this research, we delineated irrigated croplands within the extent of cropland. The definition of cropland was the same as that of the Joint Experiment of Crop Assessment and Monitoring (JECAM) network for Group on Earth Observations Global Agricultural Monitoring Initiative (GEOGALM), which defines the land used for seasonal crops (sowed/planted and harvested at least once within 12 months), such as cereals, root and tuber crops, for oil crops, and for economically significant crops,

such as sugar, vegetables, and cotton (Waldner et al., 2016). Additionally, the land occupied by greenhouses was considered cropland. To achieve comprehensive global cropland coverage, the synthesized data were obtained from 16 recent national and regional datasets spanning 2015-2019, which were supplemented by two global satellite-derived land cover datasets, as listed in Table 2. In this study, all land cover classes that met the cropland definition were consolidated into a single category labelled "cropland." On the other hand, various nonvegetation land cover classes (e.g., urban or water) and vegetated classes (e.g., forest or grasslands), including agricultural categories (e.g., permanent crops, cultivated rangeland, and grassland), were amalgamated into one class as "noncropland." The cropland mask at a 30-metre resolution could be obtained from the International Research Center of Big Data for Sustainable Development Goals via https://data.casearth.cn/thematic/cbas_2022/158. This data integrated more than 10 cropland dataset including global cropland product: FROM-GLC, GFSAD30 as well as National and regional data sets, such as ChinaCover (Wu et al., 2017; Wu et al., 2024), Cropland Data Layers (Boryan et al., 2011), Agriculture and Agri-Food Canada Annual Crop Inventory (Fisette et al., 2013; Mcnairn et al., 2009), MapBiomass (Do Canto et al., 2020) et.al. More information about this cropland mask can be found in supplementary. These data have been utilized for their extensive validation by local experts, leading to their high precision in mapping cropland (Wu et al., 2023a). The overall accuracy of this cropland was 89.4%. Moreover, this mask has also been employed in other studies to map global crop intensity (Zhang et al., 2021a).

2.4 Irrigation mapping method

2.4.1 Identifying the dry months and dry years

The cumulative yearly rainfall and monthly rainfall (P) for 2010-2019 were calculated from the TRMM dataset for all the IMZs via GEE. Simultaneously, monthly potential evapotranspiration (PET) for the same time was derived from the MOD16A2.006 product in GEE. The monthly water surplus (P - PET) was established as the difference between the monthly P and the monthly PET.

Within the growing seasons of 2017-2019, we identified the dry months by pinpointing the lowest differences between the monthly P and PET. Additionally, we determined the driest year from 2010-2019 based on the lowest annual P, and the corresponding driest month was identified as the month with the lowest P-PET value during the driest year within the growing season.

2.4.2 Identifying thresholds of NDVI and NDVI deviation

Irrigated cropland is characterized as cropland subjected to human interventions and equipped with irrigation infrastructure, including systems such as canals and CPISs (Wu et al., 2023a). The specific threshold for distinguishing between irrigated and nonirrigated cropland differs among IMZs. The threshold for each IMZ was determined by training samples through visual interpretation of very high-resolution images from Google Earth.

For each IMZ, the maximum NDVI was calculated within the cropland extent during the dry month (NDVImax-DM) by using Landsat-8 images in Google Earth Engine to detect vegetation signals. In regions where regular irrigation is necessary, irrigated cropland can be mapped annually. However, to avoid missing fallow land based on the results of a single year, the irrigated lands represented irrigated croplands identified through the NDVI threshold over a three-year period from 2017 to 2019.

For regions with ample rainfall, drought stress may not be a concern. Hence, satellite data spanning the 2010-2019 period were utilized to identify the crop conditions during extreme drought events. The NDVI deviation ($NDVI_{dev}$) was calculated for the driest month of the driest year from 2010-2019 for the cropland pixels according to the following formula:

$$NDVI_{dev} = \frac{\mathrm{NDVI}_{\mathrm{max-DriestM}} - 10\mathrm{YNDVI}_{DM}}{10\mathrm{YNDVI}_{DM}} \quad (1)$$

where $\mathrm{NDVI}_{\mathrm{max\text{-}DriestM}}$ is the maximum NDVI value in the driest month over 10 years, and $10\mathrm{YNDVI}_{DM}$ is the monthly average NDVI in the same month.

For each IMZ, the midpoint value for a cropland pixel was determined from the irrigated and nonirrigated training points via Fisher's linear discriminant (Duda et al., 2012):

$$\mathrm{Nmidpoint} = \frac{N_{irrigated} + N_{nonirrigated}}{2} \quad (2)$$

where $N_{irrgated}$ and $N_{non-irrgated}$ represent the mean values of the NDVI or $\mathrm{NDVI}_{\mathrm{dev}}$ at irrigated and nonirrigated points, respectively.

For each IMZ, the Nmidpoint, which serves as the threshold value, of the NDVI value and $\mathrm{NDVI}_{\mathrm{dev}}$ was computed using irrigated and rainfed samples. Subsequently, pixels exhibiting an NDVI exceeding their specific threshold values for dry months or an $\mathrm{NDVI}_{\mathrm{dev}}$ less than the threshold during the driest month of the driest year were designated irrigated; otherwise, the pixels below the threshold were classified as nonirrigated.

The final threshold value was determined by selecting the NDVI or $\mathrm{NDVI}_{\mathrm{dev}}$ threshold that yielded the highest overall accuracy in distinguishing irrigated cropland in the validation samples. Subsequently, the chosen threshold value for either the NDVI or $\mathrm{NDVI}_{\mathrm{dev}}$ of the IMZ was applied to the respective pixels, which were accepted as the final results. If the maximum NDVI value in the dry month achieved greater accuracy for identifying irrigated cropland, the corresponding region usually needs regular irrigation and thus is labelled as region irrigation regular (RIR). Otherwise, the region needs irrigation only occasionally for some years and thus is labelled as region irrigation occasional (RIO).

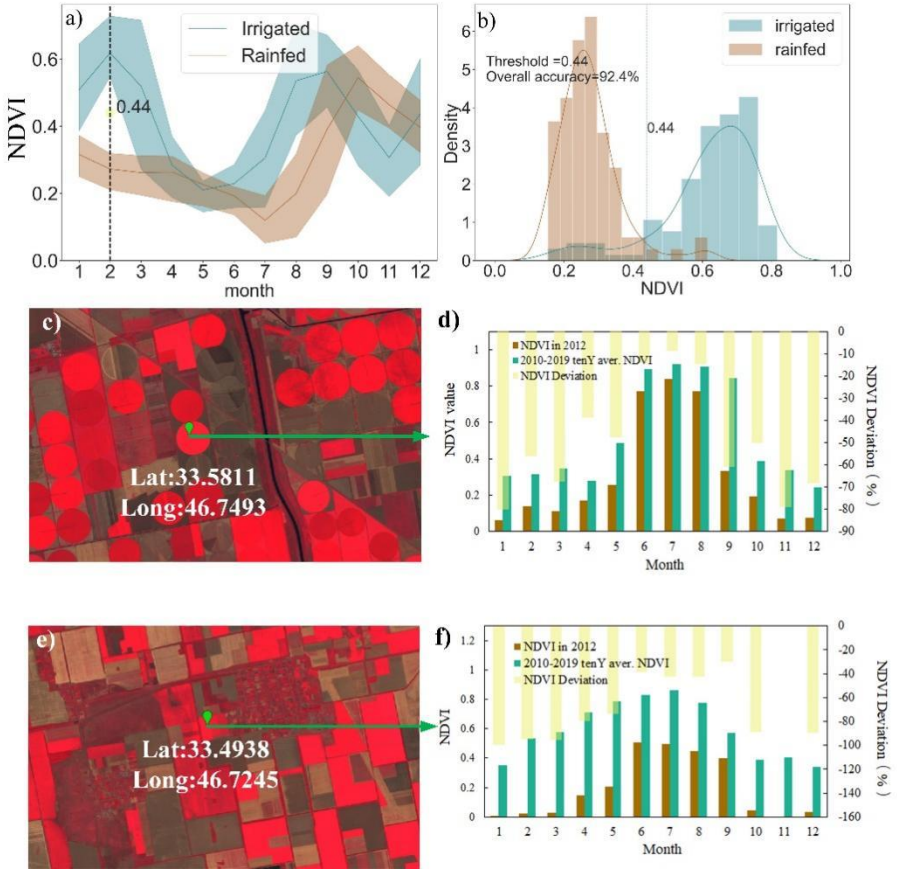

Figure 3. NDVI profile in 2017 (a); NDVI histogram in February 2017 (b) (Pakistan IMZ C48 as an example); monthly NDVI in an extremely dry year (2012), ten-year average NDVI, and $NDVI_{dev}$ for typical central pivot irrigated cropland (c, d) and rainfed cropland (e, f) in southern Ukraine (IMZ C58). The background images in c and e are Landsat-8 images. c and e are credited to @U.S. Geological Survey

Taking IMZ C48, primarily situated in Pakistan, as an example, Figure 4a illustrates the monthly NDVI profile for the year 2017 within Pakistan (IMZ C48, South Asia Punjab to Gujarat). It is evident that the discrepancy in NDVI values between irrigated and nonirrigated crops remained marginal for the majority of the months in 2017. However, in February 2017, during a period of drought stress characterized by a meagre precipitation of 4.4 mm or a precipitation-to-evapotranspiration ratio of 0.02, the disparity in NDVI values became notably more pronounced and distinguishable. Consequently, the optimal NDVI threshold of 0.44 was ascertained to be the most suitable for discriminating irrigated from nonirrigated regions, as depicted in Figure 4b.

For the RIO, IMZ C58 was chosen as an example. Figure 3d and f show the monthly NDVI profiles for the extreme drought year of 2012, the ten-year average NDVI value, and the NDVI deviation of the extreme drought year from the ten-year average. The comparison revealed that rainfed cropland exhibited more substantial fluctuations in the NDVI than did irrigated cropland. Consequently, the $NDVI_{dev}$ (NDVI deviation) during severe drought or extremely arid conditions was

employed to differentiate irrigated cropland from other categories. The $NDVI_{dev}$ midpoint was established as 0.12 following equation (2).

By amalgamating these two categories of irrigated cropland, we created a comprehensive global irrigation map. For further detailed information, please refer to (Wu et al., 2023a). Originally, the Global Maximum Irrigated Extent (GMIE) dataset was established at a 30-metre resolution, featuring a binary classification into irrigated and rainfed cropland. This resolution was determined by the availability of cropland masks and NDVI data, both of which are at the 30-metre scale. However, the extent of irrigation may vary due to crop rotation and fallow cropland, which can be distinctly observed at a 30-metre resolution and impact the extent of irrigated cropland. We calculated the irrigated cropland proportion within 100 m ×100 m to reduce these effects. The GMIE-100 dataset ranges from 0 to 1, with a no-data value set at -99.

2.5 Irrigation method identification

Motivated by the spatial attention gate, four attention blocks were incorporated into the connections between downsampling and upsampling within the U-Net architecture (Figure 4). Pivot-Net includes four spatial attention gates to effectively capture information pertaining to the round shape of the CPIS. To enhance model comprehension of shape-related intermediate representations during boundary detection and segmentation tasks, a multitask learning approach was employed to train the model. This approach encompasses pixelwise segmentation and boundary prediction as integral components of Pivot-Net's learning objectives. This method was successfully applied in identifying CPIS for the whole US (Tian et al., 2023b).

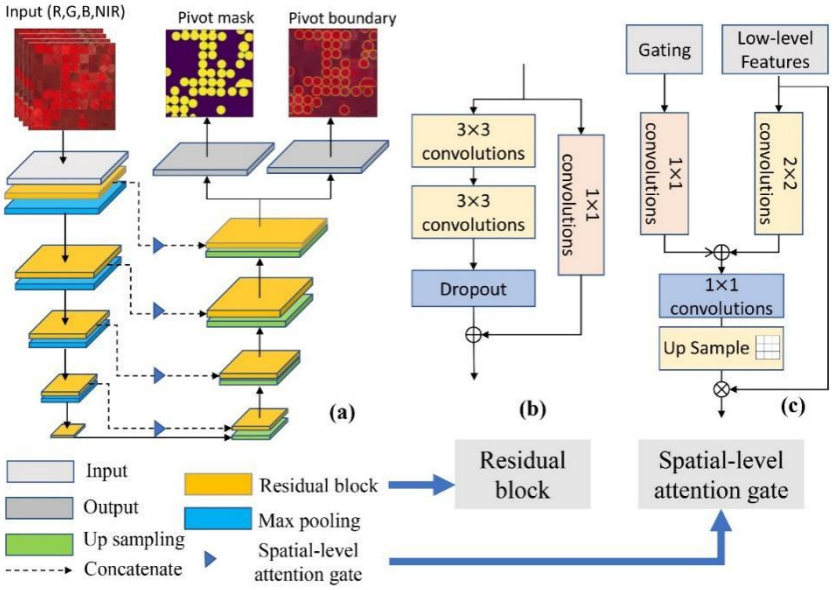

Figure 4 Architecture of the shape-attention Pivot-Net (Tian et al., 2023b).

We generated composite, cloud-free satellite data by utilizing optical images from Sentinel-2 and Landsat-8 for each tile within GEE from March to August 2020. All exported data from GEE were stored in Google Drive. The world was divided into 345 6°×6° tiles, 23 of which were annotated manually (Figure 5). Eighty percent of all the CPIS labels or 9140 patches with 256×256 pixels were used for training the model, and the remaining 20% of the CPIS labels or 2284 patches were used for accuracy validation.

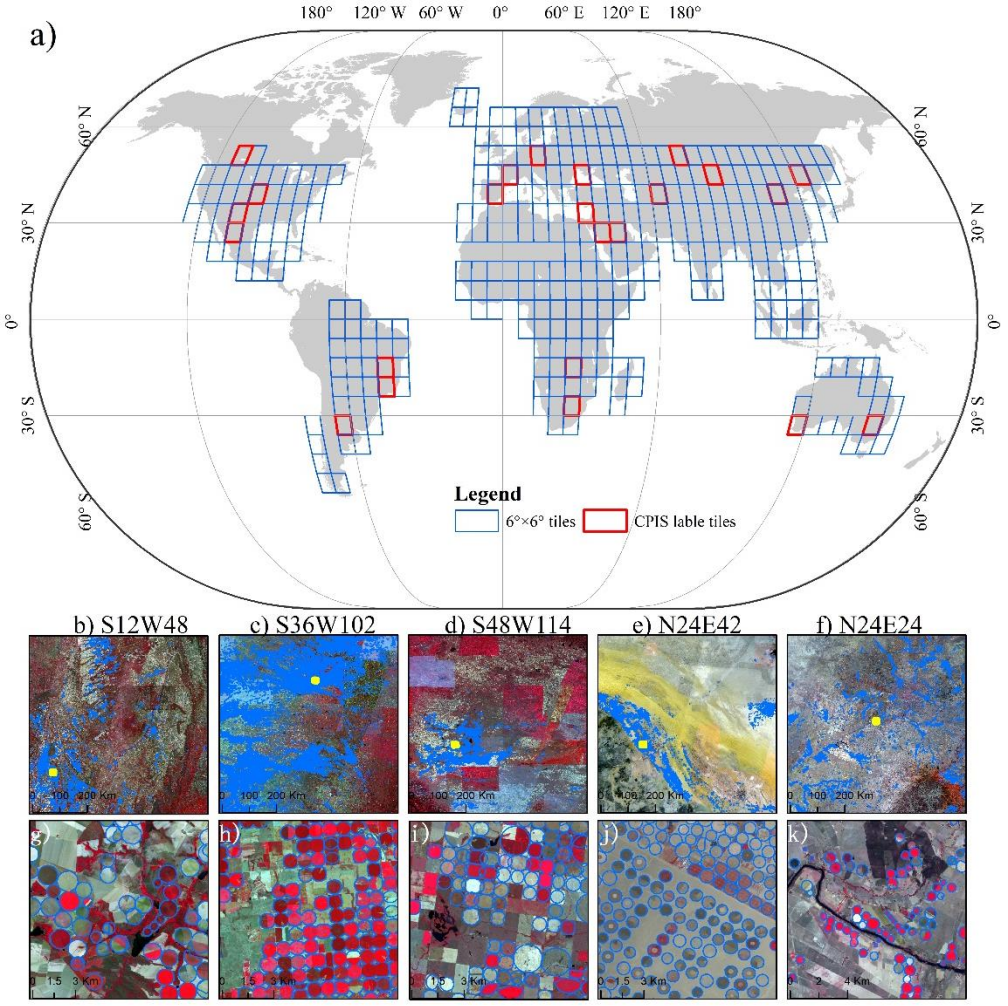

Figure 5 a) Distribution of irrigation mapping zones and irrigated and rainfed cropland samples. b-f) 5 annotated tiles for CPIS labels and images. b-f are the coordinates of the lower left corner point of each tile. g-k are detailed maps of CPIS labels. Their locations are shown in b-f) as yellow rectangles. The background images in b-k are Landsat-8 images.

Subsequently, we transferred the trained model, which was stored on a local high-performance computer, to Google Drive. By employing the robust computational capabilities of Google Colab Pro+ (https://colab.research.google.com/), which

seamlessly accesses satellite data in Google Drive, we applied the well-trained Pivot-Net model across all tiles. The satellite data were partitioned into 256×256 patches with a 128-pixel overlap (Stride = 128 pixels). The final prediction was determined by selecting the maximum prediction probability within the overlap region.

3. Results and Discussion

3.1 Spatial pattern of irrigated cropland and GCPIS

The spatial distribution of GMIE-100 is depicted in Figure 6. The GMIE-100 revealed that the maximum extent of irrigated cropland is 403.17±9.82 million hectares (Mha), which accounts for 23.4%±0.6% of the global cropland, equivalent to 1,724.08 Mha. This figure surpasses the total area equipped for irrigation reported by FAOSTAT for 2000–2008 (307.60 Mha) (Siebert et al., 2013) and closely aligns with the irrigated area estimated by IWMI–GIAM (406.40 Mha, representing 19.5% of global cropland in 2000) (Thenkabail et al., 2009). India (94.85 Mha, representing 50.4% of cropland) has the largest area of irrigated cropland in the world, with China (85.16 Mha, 50.0% of cropland) and Pakistan (18.04 Mha, 80.2% of cropland) ranking 2nd and 4th, respectively. In addition, the United States (26.54 Mha, 15.5% of cropland) ranks 3rd globally in terms of irrigated cropland. For the remaining countries, less than 10 million hectares of cropland are irrigated.

The irrigated cropland is notably concentrated in regions characterized by expansive plains and proximity to rivers. These flat and river-proximal areas are well suited for irrigation due to easy access to water resources (Jianxi et al., 2015; Bingfang Wu et al., 2021). In fact, a substantial portion of the global irrigated cropland, encompassing 224 million hectares, or 55.6% of the total irrigated cropland, is situated in such plain regions. Prominent examples include the Ganges Plain, the Indus Plain, and the North China Plain, all of which host significant expanses of irrigated cropland. Nevertheless, despite their close proximity to water sources, there are areas where the proportion of irrigated land remains low. For instance, regions such as the Danube estuary in Romania exhibit an irrigation proportion of 3.65%, despite experiencing high annual food production variability (Wriedt et al., 2009). Similarly, the Zambezi basin, which encompasses countries such as Zambia (4.1%) and Mozambique (4.2%), struggles with food insecurity despite its access to water resources.

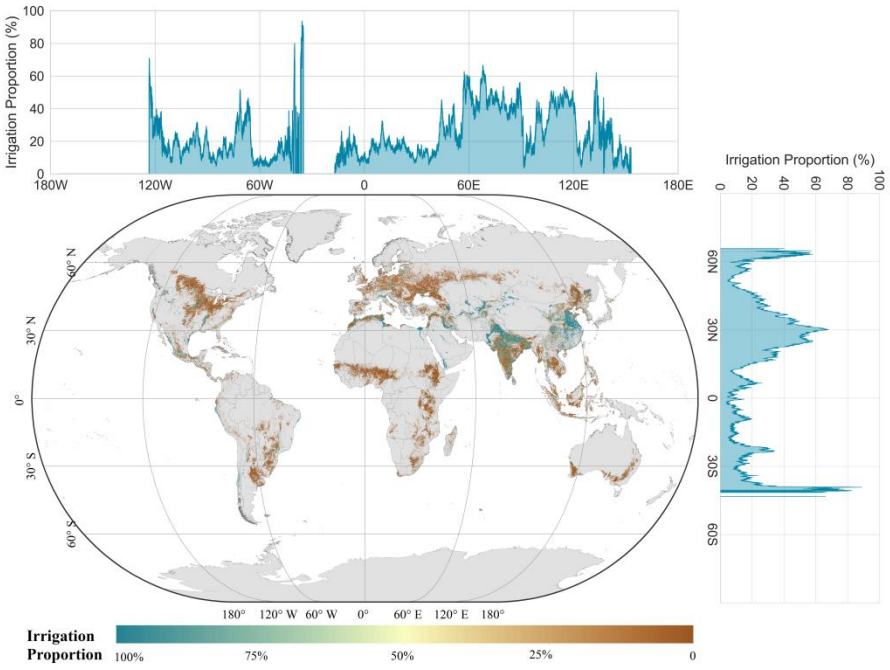

Figure 6 Global dataset of 100 m resolution irrigated cropland proportions.

Apart from plains, oases within arid zones represent a significant category of regions with extensive irrigated cropland. These areas are distinctive due to their limited precipitation but abundant sunlight and heat resources (Chen et al., 2023b). In oases, the availability of irrigation is crucial for crop survival. Approximately 31 million hectares of irrigated cropland are situated within arid zone oases, constituting 7.7% of the total irrigated cropland. Well-known oasis agricultural regions across the world include the Nile basin and the delta region in Egypt, the California Valley in the USA, and Xinjiang in China. These areas thrive due to their irrigation practices, which enable the productive use of scarce water resources amid arid conditions (Cui et al., 2024).

The distribution of irrigated cropland exhibits distinct patterns when examined from both latitude and longitude perspectives. Along the latitudinal axis, we observe exceptionally high irrigation proportions around the 30°N latitudinal line, which encompasses regions along the lower Yangtze River, Ganges River, Indus River, and Nile River. These river basins are characterized by dense concentrations of irrigated cropland, owing to the availability of water resources from these major river systems (Nagaraj et al., 2021). On the other hand, when assessing irrigation proportions along the longitudinal axis, we observe elevated levels of irrigation between 60°E and 120°E. This longitudinal span encompasses prominent regions such as the Indus-Ganges Plain and the North China Plain, which are renowned for their high levels of irrigated agriculture.

For the CPIS worldwide, the spatial pattern is depicted in Figure 7. The total area of the CPIS is estimated to be 115,192.2 ±100.0 km^2, comprising 2.9% of the total irrigated area. The area in Chen's research is 107,232.8 km2 (Chen et al., 2023a) in

global arid regions. The CPIS is mainly distributed in the high plain aquifers (HPAs), including north Texas, Kansas and Nebraska, southern Brazil, South Africa, and the middle east region. Along the longitude, the CPIS proportion is high from 90°W to 120°W, which matches the range of HPA, while the CPIS proportion is relatively apparent between 30°N and 60°N with latitude.

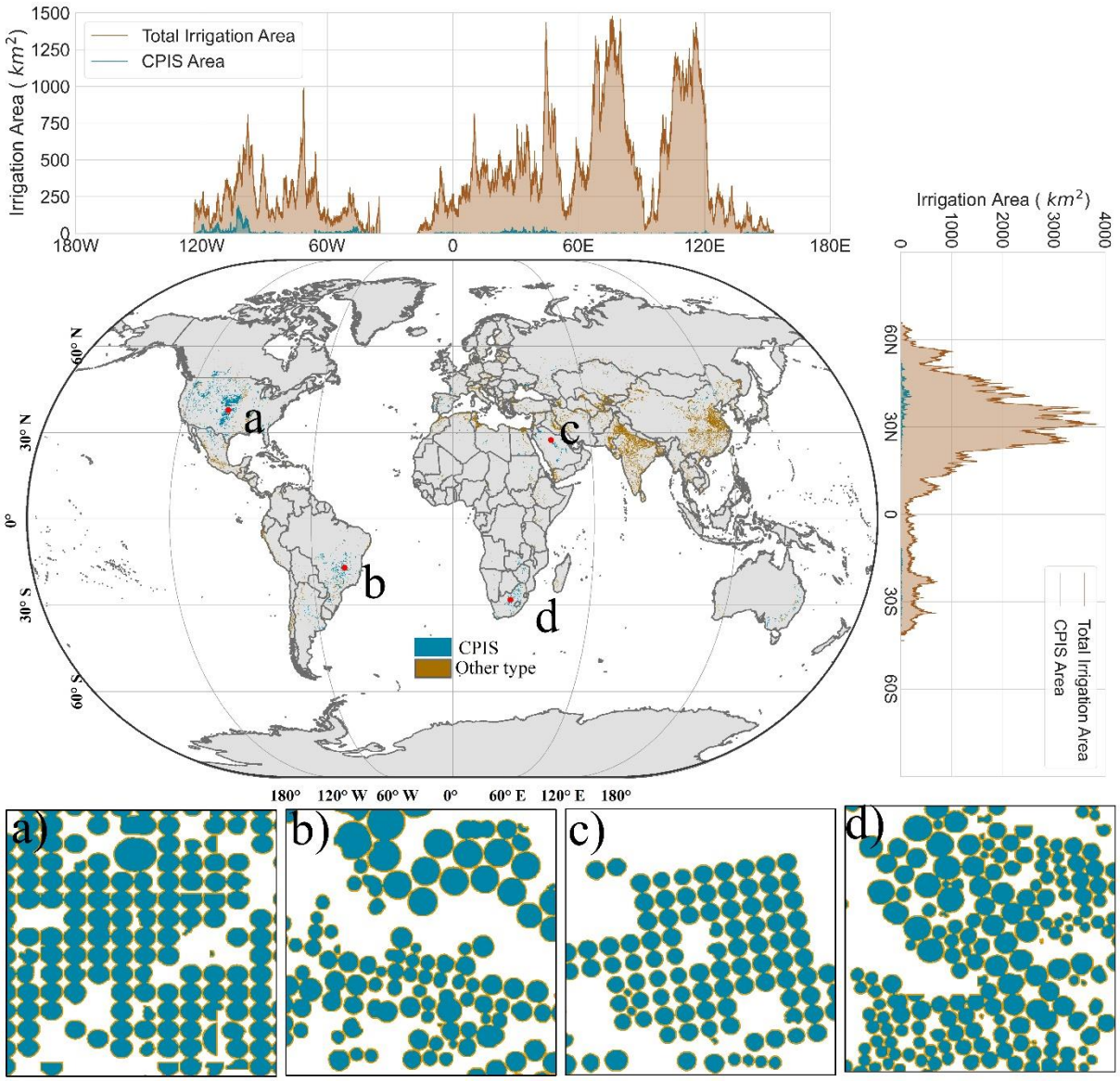

Figure 7 The distribution of irrigation types within the irrigation extent. Figure b to d are the detail map of CPIS. The location of each sub figure was labelled in the main global map.

The distributions of irrigated cropland and CPIS proportions across the six continents are depicted in Figure 8a. Asia has the most irrigated area, covering 273.79 million hectares (Mha), with an irrigation proportion of 39.3%. North America followed with 16.9%, South America with 15.5%, Europe with 10.6%, Africa with 9.6%, and Oceania with 9.2%. For the irrigation method, the CPIS proportion was highest in North America, with CPIS accounting for 13.8% of the total irrigated area, followed by South America at 5.0% and Oceania at 2.9%.

In Figure 8b, we summarize the irrigation and CPIS proportions across different climate zones. We used the global aridity index and criteria in the literature to classify climate zones (Zomer et al., 2022). The irrigation proportion decreases significantly, from 91.8% in hyperarid zones to 20.7% in semihumid zones. It then exhibits a slight increase to 21.4% in humid zones. These variations in irrigation proportions correspond to the distinct water availability and climatic conditions in these regions. For the irrigation method, the CPIS proportion is highest in the hyperarid region (5.7%), followed by the semiarid region (3.9%).

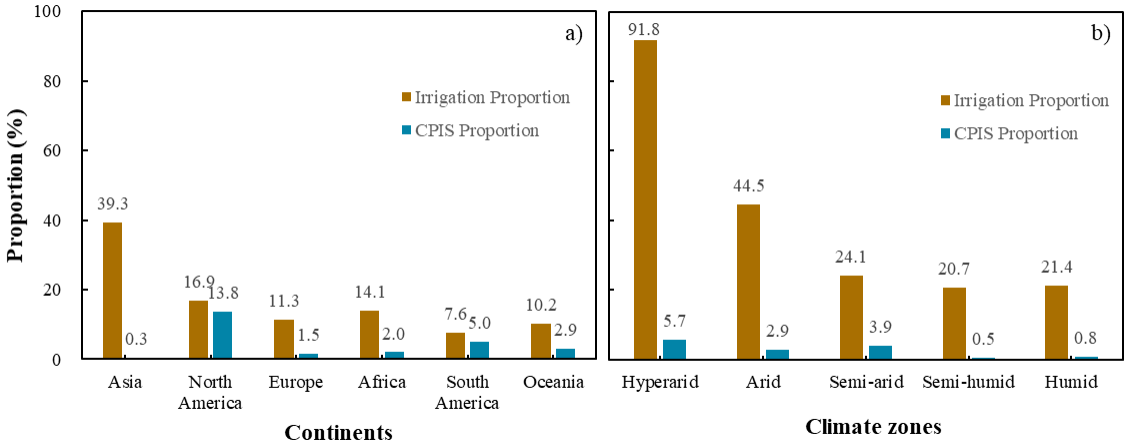

Figure 8 The irrigation proportion and CPIS proportion of total irrigated area for continents (a) and climate zones (b)

Figure 9a shows the irrigation proportion for each country. Notably, the irrigation proportion increases with geographical expansion from North Africa through West Asia, South Asia, and East Asia. In Figure 9b, the irrigation proportions are presented for each IMZ. The spatial distribution aligns with the pattern depicted in Figure 9a. Several countries in West Asia and North Africa, including Oman, Saudi Arabia, Qatar, and Egypt, boast irrigation proportions of 100%. Additionally, three countries surpassed an irrigation proportion of 80%, namely, Turkmenistan (89.4%), Uzbekistan (81.3%), and Pakistan (80.4%). Among all the AEZs, Gansu-Xinjiang in China has the highest irrigation proportion at 100.0%, followed by the Central Northern Andes (96.2%), Old World Deserts (90.5%), Southern Himalayas in India (84.0%), Semi-Arid Southern Cone (82.9%), and China Lower Yangtze (80.8%).

Figure 9c and 8d are the CPIS proportions for each country and the IMZ, respectively. CPISs are mainly concentrated in countries with intensified agricultural regions and extreme arid zones, such as the Middle East. The highest proportion of CPIS is in Namibia (23.4%), followed by the US (20.33%), Saudi Arabia (16.3%), South Africa (15.7%), Canada (12.6%), Zambia (12.5%), the Gaza Strip (12.2%) and Brazil (9.6%). For the IMZs, the proportions of CPIS were greatest in the Amazon (C24) at 81.2%, north of the High Plains (C12-4) at 42.5%, South Zambia (C09-3) at 41.6%, American northwestern Great Plains (C12-3) at 36.0%, Western Mongolia (C47) at 25.0%, British Columbia to Colorado (C11) at 24.2%, American cotton belt to the Mexican coastal plain (C14-1) at 22.8%, and the southwest Mexican and northern Mexican highlands (C18) at 21.4%.

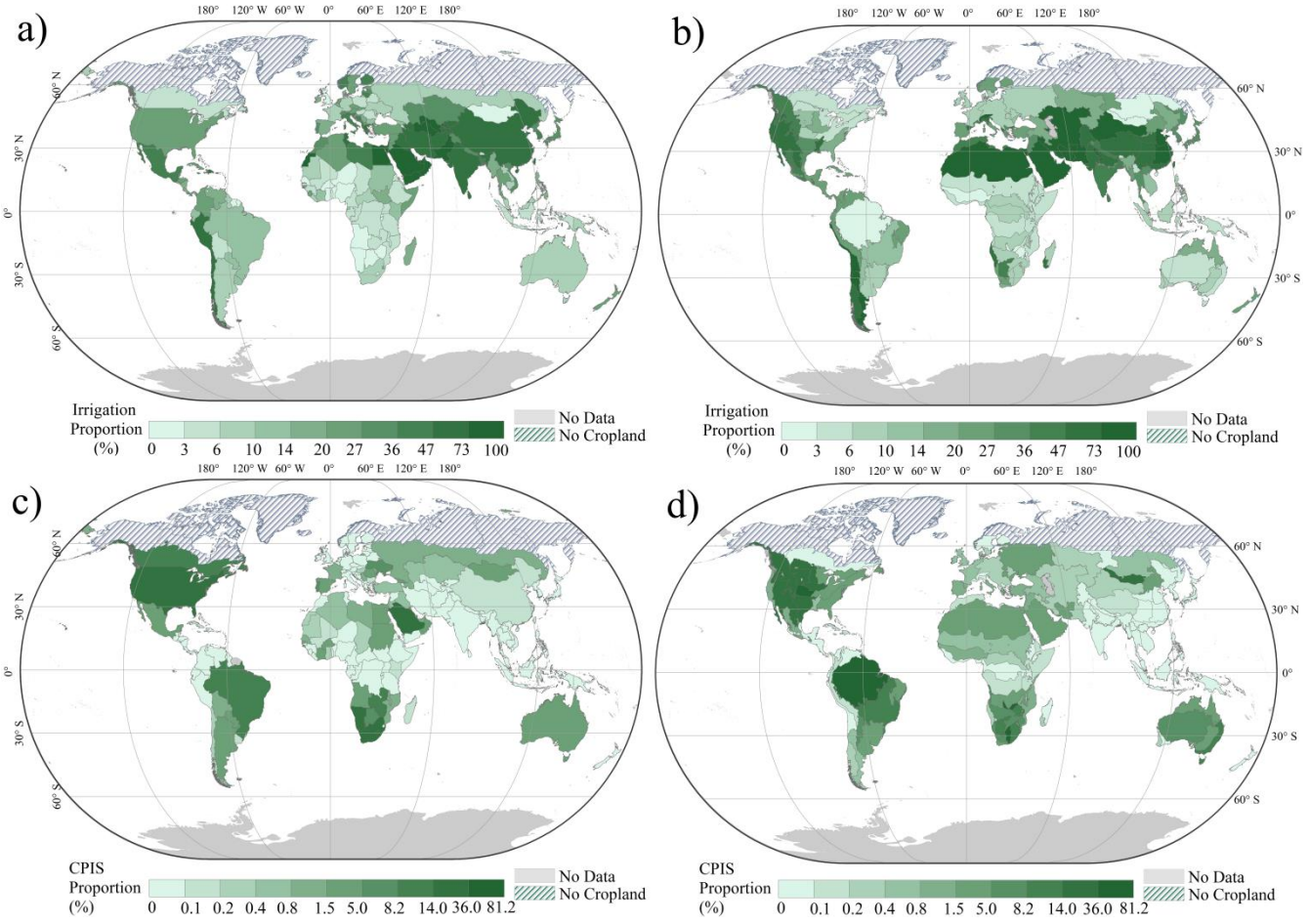

Figure 9 The irrigation proportion for each country (a) and IMZ (b) and the CPIS proportion of total irrigated cropland for each country (c) and IMZ (d)

3.2 Reliability of the GMIE-100

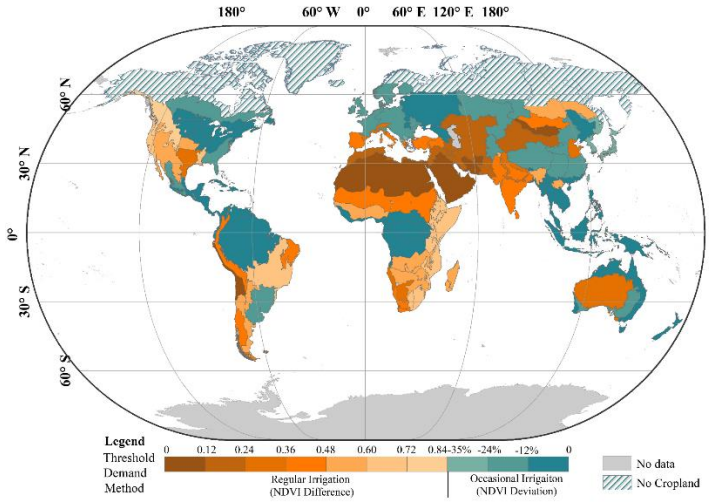

Figure 10 The thresholds of the NDVI difference and deviation for each IMZ

For each IMZ, the irrigation mapping method and threshold of the NDVI or $NDVI_{dev}$ are shown in Figure 10. For the IMZ with a regular dry season, the NDVI difference method was employed to determine the difference in amplification conditions between irrigated and rainfed cropland. To avoid the omission of fallow land and crop rotation, the maximum NDVI in the dry months of 2017-2019 was selected. The NDVI threshold for each IMZ was determined using training samples, which ranged from 0.10 in extremely arid regions, such as the Old-World Deserts (IMZ C64), to 0.74 in British Columbia to Colorado in North America (IMZ C11), as shown in orange in Figure 10. These thresholds are integral to the accurate identification of irrigated cropland within each IMZ.

For regions without a significant dry season, the driest month of an extremely dry year among the 10 years (2010-2019) was selected to amplify the crop conditions between irrigated and rainfed cropland. The $NDVI_{dev}$ was calculated as a proxy of crop condition departure from the 10-year average by using collected training samples. The values ranged from −1.0% (Amazon, C24) to −37.0% (C60-10, northwestern Greece and southwestern Albania), as shown in blue in Figure 10.

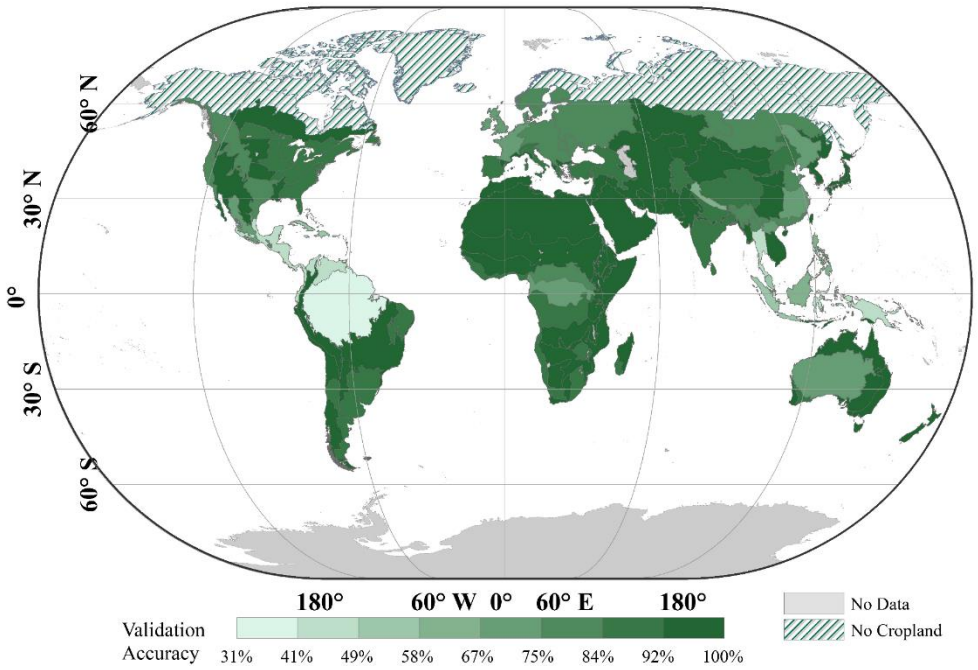

Figure 11 Training accuracy for each irrigation map zone

Figure 11 is the training accuracy of each IMZ. The NDVI or $NDVI_{dev}$ threshold was determined using the Fisher discrimination method with 92,303 obtained samples. Then, the training accuracy was assessed, which was between 0.31% in the Amazon (C24) and 100% in Western Asia (C31-2). Despite the accuracy in some humid regions, such as northern South and Central America (42%) and the Caribbean (49%), there are 89 IMZs with accuracies greater than 80% among the 105 IMZs with cropland. The confusion matrix accuracy metrics of GMIE-100 are shown in Table 2. To validate the final accuracy of the GMIE-100, the remaining 20% of the samples or 23,076 points were used. The overall accuracy of GMIE-100 was 83.6%, with a user accuracy of 86.1% and an accuracy of 82.2%.

Table 2 Confusion matrix and accuracy assessment of GMIE-100

		Field points			
	Classes	Rainfed	Irrigation	Total	User accuracy
Predicted	Rainfed	9,270	2,170	11,440	81.0%
	Irrigated	1,622	10,014	11,636	86.1%
	Total	10,892	12,184	23,076	
	Producer accuracy	85.1%	82.2%		
Overall Accuracy:		83.6%			

The accuracy of GMIE-100 was evaluated in 10 countries, and the results are presented in Figure 12, which shows the overall accuracy, user accuracy and producer accuracy for each country. In China, the accuracy was assessed using 13,963 ground truth data points from multiyear GVG data. The overall accuracy was 85.5%, with a predicted accuracy of 86.7% and user accuracy of 83.3%. Commissions and omissions were common in humid areas, such as southern China, Cambodia and Myanmar. In other countries, the overall accuracy of the GMIE-100 datasets was basically acceptable.

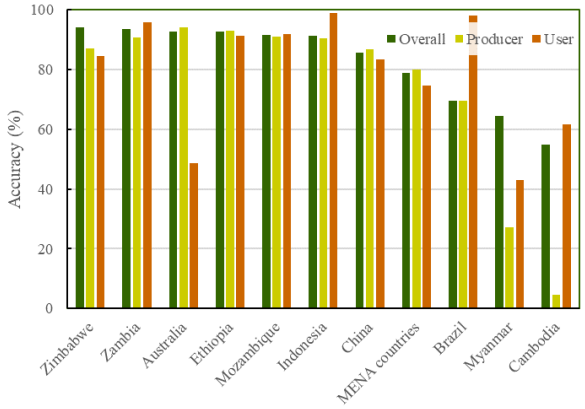

Figure 12 Accuracy for countries with GVG (GPS, Video, GIS) irrigation validation points

The accuracy metrics and confusion metrics for the CPIS are listed in Table 3. The model achieved a high validation accuracy of 97.87%±0.1%. The F1 score, which is a balance between precision and recall, is 86.87%±0.1%. The mean intersection over union (IOU) is 87.25%±0.2%. We visualized four patches with dense CPIS in Figure 13. Overall, the CPIS is well identified in most cases.

Table 3 Confusion matrix of GCPIS identified with Pivot-Net

		CPIS Predict		Recall
		0	1	
CPIS Label	0	119938874	735300	
	1	2077463	9303403	81.75%±0.2%
Precision			92.68%±0.1%	
Overall Accuracy				97.87%±0.1%

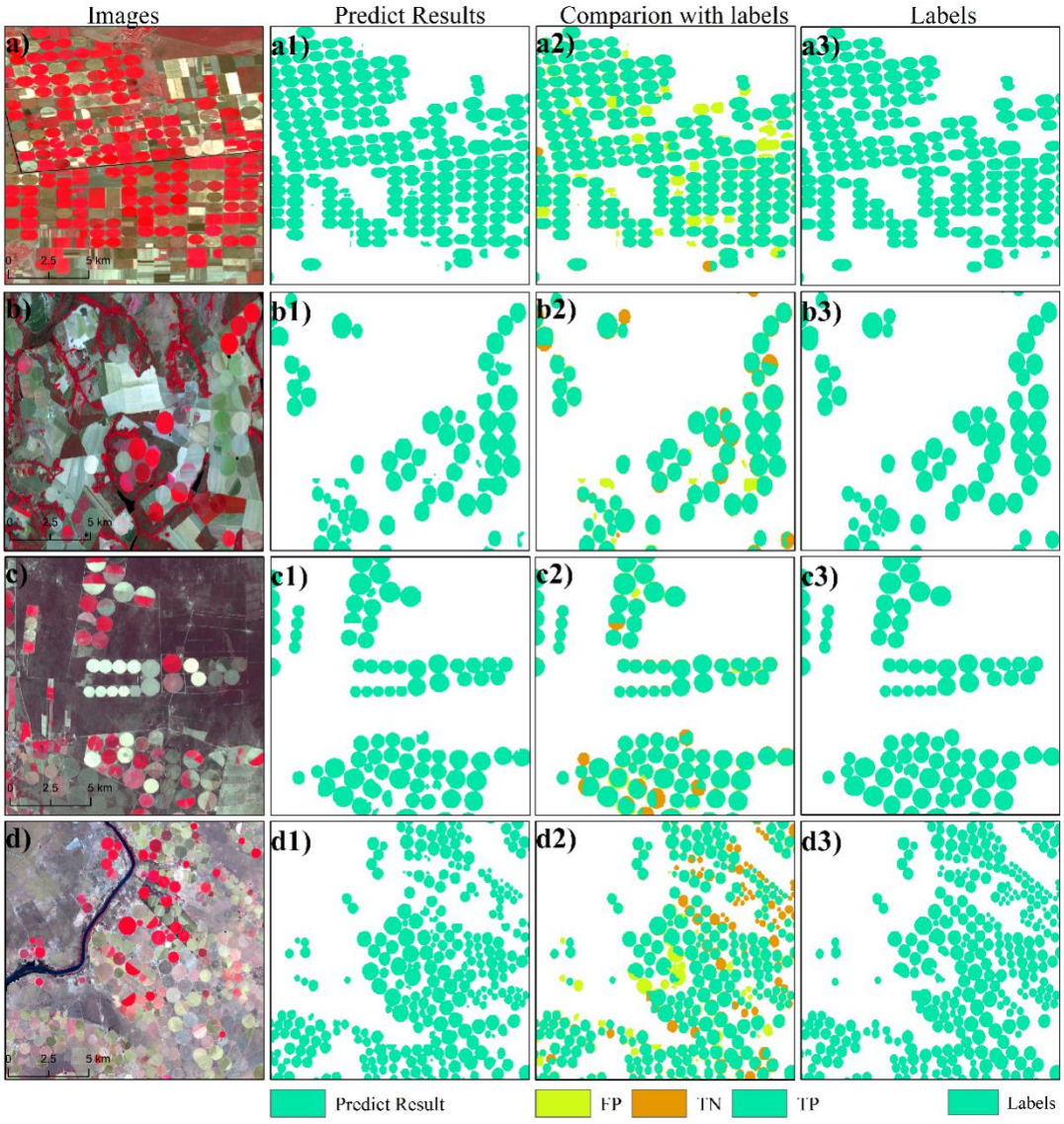

Figure 13 Accuracy assessment for the CPIS identification results. a-d are the composted images; a1-d1 are the prediction results of Pivot-Net; a2-d2 are the comparisons between our results and the labels. TP represents true positive pixels, while TN represents true negative pixels. FP means false positive samples. a3-d3 are the labels. The central point coordinates of a-d are (33.86, 46.37), (-47.34, 16.41), (-65.74, 32.03), and (25.11, 28.06), respectively. The background images in a-d are Landsat-8 images. a-d are credited to @U.S. Geological Survey

3.3 Comparison with existing irrigation datasets

3.3.1 Comparison of irrigated cropland

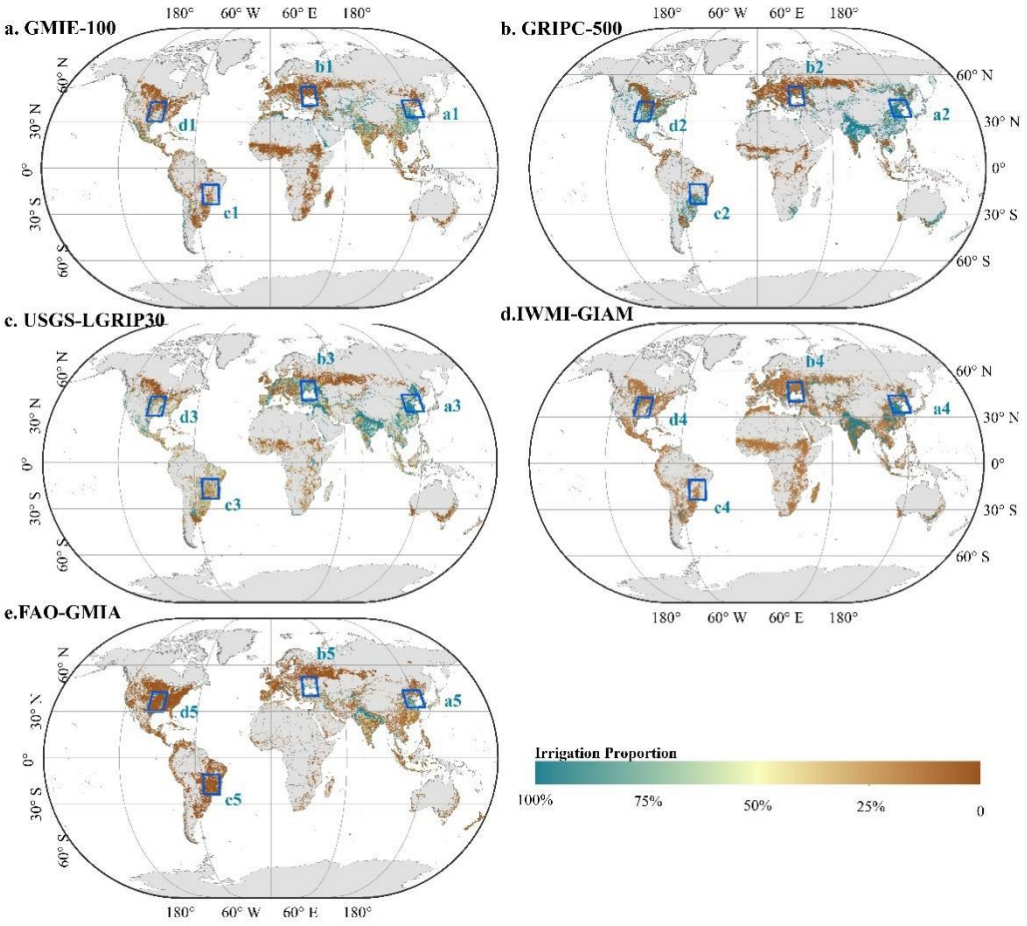

Figure 14 Comparison of existing irrigation production at 1 km (GMIE-100, GRIPC-500, USGS-LGRIPC30) or 10 km resolution (IWMI-GIAM and FAO-GMIA)

To compare GMIE-100 with four existing irrigation products, we downscaled GMIE-100 and GRIPC-500 and USGS-LGRIP30 to a 1 km resolution and scaled IWMI-GIAM and FAO-GMIA to a 1 km resolution via the bilinear interpolation method. The results are shown in Figure 14. The spatial pattern of irrigated cropland in GMIE-100 generally coincided with that of the other products. Irrigated cropland was most concentrated in the North China Plain and Ganges & Indus River basin worldwide.

Nevertheless, there were discernible differences in the detailed distributions of irrigated cropland patches, such as those in Northeast China, the Eastern European Plain, the Planicie de la Plata of South America and the lower Mississippi River basin (Figure 15). In the Northeast China Plain, the irrigated cropland is denser in USGS-LGRIP30 and GRIPC-500 than in

the other products. According to census data from China, the average irrigation proportion for three provinces (Heilongjiang, Jilin, Liaoning Province) is 39.32%. According to the GMIE-100 results, the irrigation proportion is 27.45%, which is closer to the census data. For the irrigated cropland in the Eastern European Plain, USGS-LGRIP30 illustrates widely distributed irrigated cropland, which is significantly denser than what is portrayed in GMIE-100 and the other three datasets (Figure 15 b1-b4). Notably, the GRIPC-500 dataset indicates a considerable extent of irrigated cropland in the Planicie de la Plata region when compared to GMIE-100 and the other products (Figure 15 c1-c4). According to census data from Brazil, the reported irrigation proportion is 6%, whereas it is 58% and 72% in USGS-LGRIP30 and GRIPC-500, respectively.

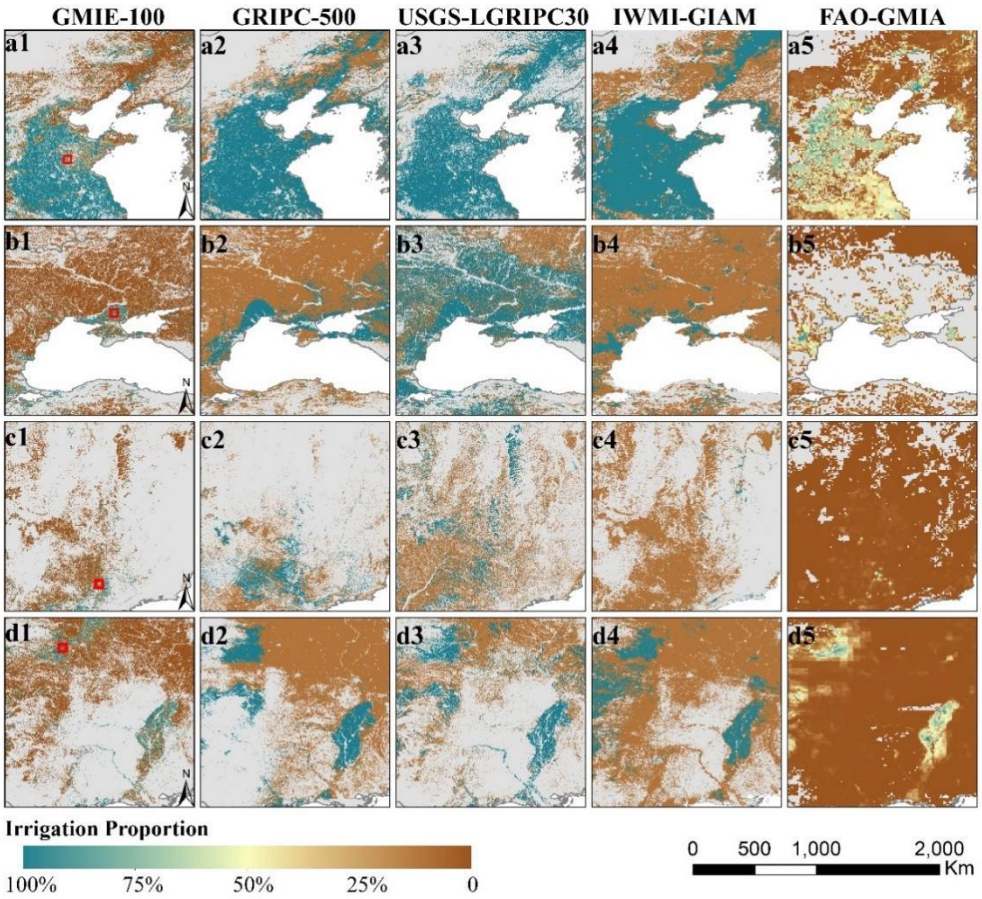

Figure 15 Comparison with existing irrigation production for the hot-point region of irrigation. The corresponding location is labelled in Figure 14 with a blue rectangle.

To validate the proposed GMIE-100, we compare it with national census data. The results are shown in Figure 16. For comparison with existing global irrigation products, we also compared GMIE-100 with FAO-GIAM, IWMI-GMIA, USGS-LGRIP30 and GRIPC-500. The R^2 between the GMIE-100 and 23 national census datasets was 0.92, with an RMSE of 3.52% and an MAE of 2.74%. For FAO-GIAM and IWMI-GMIA, the R^2 values with GMIE-100 were0.72 and 0.73, respectively.

The determination coefficient between USGS-LGRIP30 and GMIE-100 was only 0.45, with an RMSE of 35.6%, the lowest value among these three existing irrigation products. When we compared USGS-LGRIP30 with the national census, the R^2 was only 0.25. When comparing GMIE-100 with GRIPC-500, the R^2 was 0.51, with an RMSE of 29.89%. The scatterplot shows that GRIPC-500 was overestimated compared to GMIE-100.

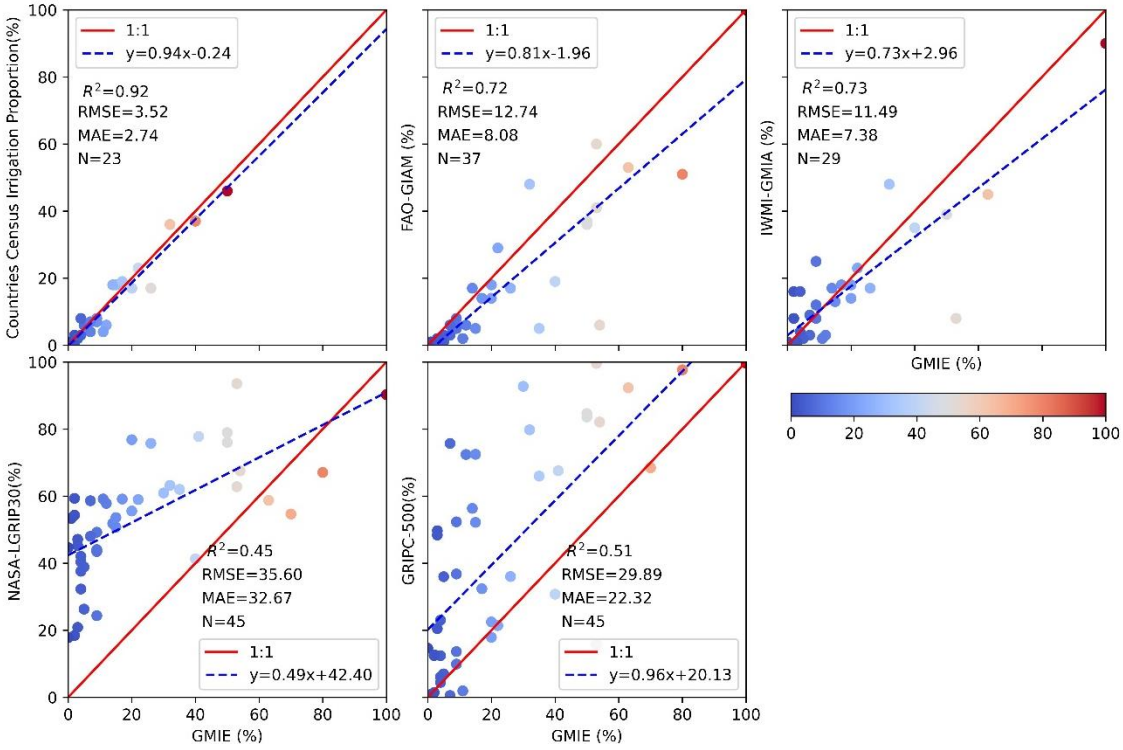

Figure 16 Comparison of national irrigation proportions between GMIE-100 and national census data (a), FAO-GMIA (b), IWMI-GIAM (c), USGS-LGRIP30 (d) and GRIPC-500 (e).

3.4 Advantages and limitations of GMIE-100

We used irrigation performance to map irrigation at regular intervals. Irrigation areas have a high level of variability in irrigation water use (Puy et al., 2021; Puy et al., 2022). Thus, changes in the irrigated area could reflect variations in agricultural water use, which is important for local water resource management. Due to a lack of updated information, global maps of irrigated areas often rely on estimates from approximately 2000 (Nagaraj et al., 2021). For RIR regions, irrigation maps can be updated every three years by collecting the vegetation signal in each dry season. For RIO regions, irrigation maps can be updated every ten years based on crop status during extremely dry events. Although the irrigated cropland extent during the

dry season can be identified from 2010 to 2019, our aim was to provide the most up-to-date information based on satellite data over the 2017–2019 period.

Periodic cropland fallowing refers to the practice of not cultivating or tilling all croplands within a single year. This approach is often employed to restore soil fertility as part of a crop rotation scheme or to prevent excess agricultural production. The use of the NDVI or $NDVI_{dev}$ threshold enables the identification of only those lands that have been actively cultivated. Subsequently, these cultivated lands can be further categorized into either irrigated or rainfed land. An area is designated as irrigated if it has been cultivated at least once during the driest month over a span of three years. This criterion aids in discerning areas that are actively managed for crop production from those temporarily left fallow or unplanted.

The spatial resolution of this dataset was 100 m, which is greater than that of the dominant irrigation data map. High-resolution irrigated cropland data are essential for quantifying agricultural water use (Wu et al., 2022). The resolution of most existing irrigation data is very coarse, varying between 500 m and 10 km (Xie et al., 2019). As shown in Figure 17, GRIPC-500, IWMI-GIAM and FAO-GMIA are not able to present detailed information on irrigated cropland. Even though the resolution of USGS-LGRIPC-30 was greater than that of GMIE-100, the latter descriptions of heterogeneous irrigated cropland distributions in the North China Plain (Figure 17 a1 and a3) and the US Plateau (Figure 17 d1 and d3) were better than the former. The evapotranspiration, precipitation product with 500-meter resolution was used to determine the driest months within each IMZ. And the time period was used to detect irrigation performance and detect irrigated cropland. In each IMZ, 30-meter NDVI data was used as major input. Then to avoid effect fallow land and crop rotation, we calculate the irrigation proportion within 100 meters.

As for the maximum extent should be understood separately for RIR and RIO. For RIR, the largest area means the cropland area irrigated one time at least for last three years (2017-2019). Because we detect irrigation every year for this region. To avoid missing fallow land, we identify the largest extent for last three years (2017-2019). For RIO, it means the cropland area irrigated one time at least for last ten years (2010-2019). For RIO, irrigation occurs occasionally. We detect weather the cropland is irrigated in the driest year. But in the normal year, the irrigation maybe not necessary in this area. So, this means the largest extent area for last ten years (2010-2019). On the other hand, when we compare our result with nation census data, the result shows high consistent. Compared with USGS-LGRIP30 and GRIPC-500, our result didn't show much overestimation.

Furthermore, with the support of the DL method, we achieved CPIS mapping worldwide, which enabled our investigation of irrigation methods. We found 11.5 ± 0.1 Mha of CPISs worldwide, composing $2.90\% \pm 0.03\%$ of the total irrigated cropland. To the best of our knowledge, this is the first study in which the CPIS irrigated method was mapped, despite Chen's research on CPI mapping in global arid regions (Chen et al., 2023a). GMIE comprises both the irrigated cropland extent and some irrigation method (CPIS) distributions with relatively high resolution, thus providing subbasin water consumption and withdrawal estimations for all sectors (Wu et al., 2022). Due to the variation in irrigation efficiency for different irrigation methods, CPISs demonstrate an efficiency exceeding 80%, while gravity-flowing irrigation methods exhibit a comparatively

low efficiency of approximately 60% (Waller and Yitayew, 2016). Therefore, irrigation efficiency can be estimated in relation to irrigation methods in the future. This process could enhance the understanding of the irrigation paradox (Grafton et al., 2018), which indicates that technological advancement increases irrigation efficiency, but crop water levels do not decrease. However, this study didn't include the lateral irrigation, because the identification of irrigation method was relied on the circle shape in the satellite data and the lateral irrigation didn't show this feature. In the maximum irrigation extent, we include all the irrigation types that could mitigate water stress.

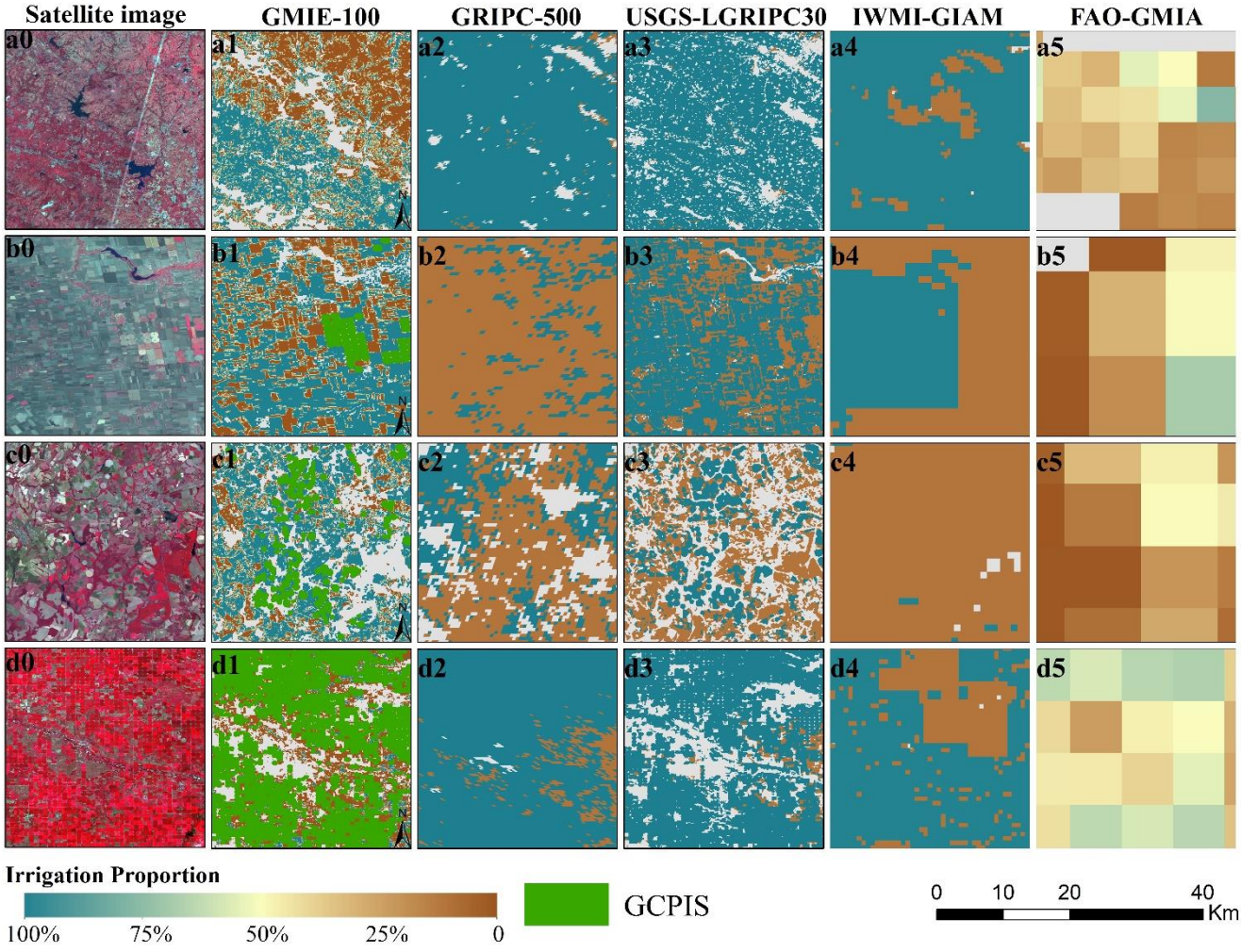

Figure 17 Comparison between GMIE-100 and existing global irrigation products in detail; their specific locations are labelled in the corresponding subfigure Figure 15 with red rectangles.

Compared to the surveillance classification method, our method requires fewer samples. However, due to a lack of expertise, all spectral characteristics of irrigated farmland were studied using training samples, which increased the required number of samples. Xie's research used 20,000 samples for irrigation mapping in the United States (Xie et al., 2019). Zhang's research used approximately 100,000 samples to identify irrigated croplands in China (Zhang et al., 2022c). By determining the NDV difference and NDVI deviation between irrigated and rainfed cropland, the required amount of training samples could be drastically reduced. In this study, a total of 92,303 samples were used to determine the NDVI threshold and the NDVI deviation threshold at the global scale. Moreover, training samples in China were mostly collected on site, which is more precise than visual interpretation.

Additionally, there are several limitations to this method. First, the accuracy of the GMIE-100 in the extremely wet season was not high because water stress seldom emerges. As a result, the accuracy of the method in some Southeast Asian countries, such as Myanmar, which has an overall accuracy of 64.5%, and Cambodia, which has an overall accuracy of 54.93%, needs further improvement. Additionally, the representativeness of sample points can be further improved, e.g., by identifying CPISs via DL methods (Tian et al., 2023b; Chen et al., 2023a), which are commonly used in the US, Brazil and the Middle East.

Second, Although GMIE-100 provides a relatively high-resolution distribution of irrigated cropland, it does produce some mixed pixels with cropland or noncropland and irrigated or rainfed cropland. This is especially true for regions with extremely small agricultural fields (Fritz et al., 2015). The cropland masks had the greatest influence on the GMIE-100 dataset (Salmon et al., 2015; Meier et al., 2018), despite the selection of 16 distinct cropland datasets derived from country- and region-level sources as high-priority inputs. These datasets often exhibit disparities in estimating the distribution of cropland, particularly in African countries, due to the complex landscape, frequent cloud cover, and the presence of small agricultural fields (Nabil et al., 2020). Consequently, inaccuracies within the cropland datasets were transposed onto the GMIE-100 dataset. Nevertheless, importantly, these datasets remain the primary sources of cost-effective and up-to-date information covering vast geographical areas. Actually, we just focus on seasonal cropland, because the permanent crops were usually for fruit trees, nut trees, coffee, tea, and some types of vines, which is recognized as shrub or tree in most landcover system such as ESRI (Karra et al., 2021), FROM-GLC (Yu et al., 2013), GLAD_Map (Potapov et al., 2022), GLC-FCS30 (Zhang et al., 2021b) and WORDCOER (Zanaga et al., 2022). On the contrary, harvest crops, maize, soybean, wheat, and rice was most important for food security. So, we choose this definition to distinguish irrigated and rainfed cropland, rather than the definition from FAO's. Different definition of crop as input data may produce varied irrigated cropland area, which will definitely introduce uncertainty in the final result. A consistent, high resolution cropland mask with high accuracy is urgently needed to solve this problem.

Thirdly, it is hard to collect the filed samples globally, we fused three sources of samples. From different country, there is varied dominant samples source. Such as in China, most of samples was obtained from GVG field survey. While in Brazil, major samples were from USGS samples. Except country with GVG and USGS-samples, the visual interpretation data was dominant sources of samples. This also ensure the represented manner of irrigated cropland. Overall, the number of samples

was very large. Basically, this irrigated and rain-fed samples database could meet the globally irrigated cropland mapping compared with global cropland expansion mapping research (Potapov et al., 2022), which achieved cropland mapping globally with thousands of samples. Meanwhile, this fused samples maybe introduce some uncertainty in terms of representation. This effect should be acceptable in arid and semi-arid regions because the irrigation performance is relatively easy to identify. However, the uncertainty maybe enlarged in wet region due to complex manner of irrigated cropland.

4. Conclusion

High-resolution and updated irrigation maps are important for tracking regional water use and food production situations. Using irrigation performance data collected during the dry season of the growing season and during extreme drought events, we produced the GMIE-100 at 100 m with the support of GEE. In this study, the entire globe was divided into 110 zones based on variations in climate and phenology. In each IMZ, we identified the dry months during the growing seasons from 2017-2019, or alternatively, the driest months during the most arid year from 2010-2019. To distinguish irrigated cropland, we employed 92,303 samples to determine thresholds for the NDVI during the dry months of 2017-2019 and the NDVI deviation from the ten-year average for the driest month ($NDVI_{dev}$). The NDVI or $NDVI_{dev}$ threshold that achieved the highest overall accuracy was selected to distinguish irrigated and rainfed cropland. All the algorithms were conducted using GEE with the code https://code.earthengine.google.com/eaafaab35dde9bbe37f443e80c716479.

With the support of the DL method, the global CPIS was identified using Pivot-Net. We identified 11.5 million hectares of CPIS irrigated cropland, accounting for approximately 2.90%±0.03% of the total irrigated cropland. However, in Namibia, the US, Saudi Arabia, South Africa, Canada and Zambia, the proportion of CPIS was greater than 10%. To our knowledge, this is the first attempt to identify irrigation methods globally, although other types of irrigation methods, such as gravity flow, are still dominant irrigation methods. However, our method can facilitate the estimation of irrigation efficiency based on different irrigation method proportions to support high-accuracy subbasin-scale water resource management.

Finally, the GMIE-100 was produced at 100 metres. Using 23,076 points to validate the results, we found that the overall accuracy of GMIE-100 was 83.6%±0.6%, but it varied among the different IMZs. The GMIE-100 indicates that the largest extent of irrigated cropland reached 403.17±9.82 million hectares, which accounts for 23.4%±0.6% of the total global cropland. Spatially, irrigated cropland is concentrated in great plains regions and regions near rivers. A total of 224 million hectares of irrigated cropland, accounting for 55.6% of the total irrigated cropland, was in the plains regions. The Ganges Plain, the Indus Plain and the North China Plain all have large amounts of irrigated cropland worldwide. The GMIE-100 provides more detailed information about irrigated and rainfed cropland and thus can better support agricultural water use estimation and regional food situation assessment.

5. Code and data availability

The data are publicly accessible through the following link: https://doi.org/10.7910/DVN/HKBAQQ (Tian et al., 2023a). The GMIE-100 dataset spans values ranging from 0 to 1, with a designated no-data value of -99. Globally, there are 67 tiles available, each with a maximum extent of 21°×21°. In cases where these tiles overlap with land, they maintain the standard extents; however, adjustments are made to the tile extents as needed to accommodate the terrestrial range. The GCPIS was stored in shapefile format in zip files. The irrigation unit zone can be downloaded from http://cloud.cropwatch.com.cn/

Author contributions

HZ and BW conceptualized the study. FT designed the experiments and carried out the experiments. BW and HZ were responsible for funding acquisition. MZ and WZ conducted the investigation and formal analysis. FT prepared the original draft of the manuscript. FT, BW, HZ, MZ, WZ, NY, YL, and YL reviewed and edited the manuscript.

Competing interests

The authors declare that they have no conflicts of interest.

Acknowledgements

We gratefully acknowledge the support of the Google Earth Engine platform, which provided essential computational and storage resources, simplifying access to archived datasets such as TM/ETM/OLI satellite data, TRMM and GLDAS for precipitation data, and MOD16A2.006 for evapotranspiration data. These resources greatly facilitated program calculations and data retrieval. We thank the data provider for the abovementioned data and the GFSAD30 team for publishing the irrigated and rainfed samples. Furthermore, we would like to express our gratitude to the authors of existing irrigation datasets, namely, GRIPC-500, USGS-LGRIP30, IWMI-GIAM, and FAO-GMIA, for their foundational work, which has significantly contributed to our research in this field. Their efforts have provided essential background information for our study.

Financial support

This research was supported by the Natural Science Foundation of China (No. 41861144019, No. 42301409), the Agricultural Remote Sensing Innovation Team Project of AIRCAS (No. E33D0201-6), and the National Key Research and Development Program of China (2016YFA0600304, 2016YFA0600302).

References

Ambika, A. K., Wardlow, B., and Mishra, V.: Remotely sensed high resolution irrigated area mapping in India for 2000 to 2015, Sci Data, 3, 160118, 10.1038/sdata.2016.118, 2016.

Bingfang Wu, Fuyou Tian, Mohsen Nabil, José Bofana, Yuming Lu, Abdelrazek Elnashar, Awetahegn Niguse Beyene, Miao Zhang, Hongwei Zeng, and Zhu, W.: Global mapping of actual irrigation capacity using the irrigation performances under drought stress capacity, Global Environmental Change (minor revision), 2021.

Boryan, C., Yang, Z., Mueller, R., and Craig, M.: Monitoring US agriculture: the US department of agriculture, national agricultural statistics service, cropland data layer program, Geocart. Internat., 26, 341-358, 2011.

Chen, F., Zhao, H., Roberts, D., Van de Voorde, T., Batelaan, O., Fan, T., and Xu, W.: Mapping center pivot irrigation systems in global arid regions using instance segmentation and analyzing their spatial relationship with freshwater resources, Remote Sens. Environ., 297, 113760, 10.1016/j.rse.2023.113760, 2023a.

Chen, P., Wang, S., Liu, Y., Wang, Y., Wang, Y., Zhang, T., Zhang, H., Yao, Y., and Song, J.: Water availability in China's oases decreased between 1987 and 2017, Earth's Future, 11, e2022EF003340, 2023b.

Chen, Y., Lu, D., Luo, L., Pokhrel, Y., Deb, K., Huang, J., and Ran, Y.: Detecting irrigation extent, frequency, and timing in a heterogeneous arid agricultural region using MODIS time series, Landsat imagery, and ancillary data, Remote Sens. Environ., 204, 197-211, 10.1016/j.rse.2017.10.030, 2018.

Cui, B., Gui, D., Liu, Q., Abd‐Elmabod, S. K., Liu, Y., and Lu, B.: Distribution and growth drivers of oases at a global scale, Earth's Future, 12, e2023EF004086, 2024.

Dari, J., Brocca, L., Modanesi, S., Massari, C., Tarpanelli, A., Barbetta, S., Quast, R., Vreugdenhil, M., Freeman, V., Barella-Ortiz, A., Quintana-Seguí, P., Bretreger, D., and Volden, E.: Regional data sets of high-resolution (1 and 6 km) irrigation estimates from space, Earth System Science Data, 15, 1555-1575, 10.5194/essd-15-1555-2023, 2023.

Deines, J. M., Kendall, A. D., Crowley, M. A., Rapp, J., Cardille, J. A., and Hyndman, D. W.: Mapping three decades of annual irrigation across the US High Plains Aquifer using Landsat and Google Earth Engine, Remote Sens. Environ., 233, 111400, 10.1016/j.rse.2019.111400, 2019.

dela Torre, D. M. G., Gao, J., Macinnis-Ng, C., and Shi, Y.: Phenology-based delineation of irrigated and rain-fed paddy fields with Sentinel-2 imagery in Google Earth Engine, Geo-spatial Information Science, 24, 695-710, 10.1080/10095020.2021.1984183, 2021.

do Canto, A. C. B., Marques, R., Leite, F. F. G. D., da SILVEIRA, J., DONAGEMMA, G., and RODRIGUES, R.: Land use and cover maps for Mato Grosso from 1985 to 2019,

Duda, R. O., Hart, P. E., and Stork, D. G.: Pattern classification, John Wiley & Sons2012.

Fisette, T., Rollin, P., Aly, Z., Campbell, L., Daneshfar, B., Filyer, P., Smith, A., Davidson, A., Shang, J., and Jarvis, I.: AAFC annual crop inventory, 2013 Second International Conference on Agro-Geoinformatics (Agro-Geoinformatics), 270-274,

Fritz, S., See, L., McCallum, I., You, L., Bun, A., Moltchanova, E., Duerauer, M., Albrecht, F., Schill, C., and Perger, C.:

650 Mapping global cropland and field size, Global change biology, 21, 1980-1992, 2015.
Gommes, R., Wu, B., Li, Z., and Zeng, H.: Design and characterization of spatial units for monitoring global impacts of environmental factors on major crops and food security, Food and Energy Security, 5, 40-55, 2016.
Gorelick, N., Hancher, M., Dixon, M., Ilyushchenko, S., Thau, D., and Moore, R.: Google Earth Engine: Planetary-Scale Geospatial Analysis for Everyone, Remote Sensing of Environment, 202, 18-27, 2017.
655 Grafton, R. Q., Williams, J., Perry, C. J., Molle, F., Ringler, C., Steduto, P., Udall, B., Wheeler, S., Wang, Y., and Garrick, D.: The paradox of irrigation efficiency, Science, 361, 748-750, 2018.
Jianxi, H., Li, L., Chao, Z., Wenju, Y., Jianyu, Y., and Dehai, Z.: Evaluation of cultivated land irrigation guarantee capability based on remote sensing evapotranspiration data, Transactions of the Chinese Society of Agricultural Engineering, 31, 2015.
Karra, K., Kontgis, C., Statman-Weil, Z., Mazzariello, J. C., Mathis, M., and Brumby, S. P.: Global land use/land cover with
660 Sentinel 2 and deep learning, 2021 IEEE international geoscience and remote sensing symposium IGARSS, 4704-4707,
Lu, Y., Song, W., Lü, J., Chen, M., Su, Z., Zhang, X., and Li, H.: A pixel-based spectral matching method for mapping high-resolution irrigated areas using EVI time series, Remote Sensing Letters, 12, 169-178, 2021.
McDermid, S., Nocco, M., Lawston-Parker, P., Keune, J., Pokhrel, Y., Jain, M., Jägermeyr, J., Brocca, L., Massari, C., Jones, A. D., Vahmani, P., Thiery, W., Yao, Y., Bell, A., Chen, L., Dorigo, W., Hanasaki, N., Jasechko, S., Lo, M.-H., Mahmood, R.,
665 Mishra, V., Mueller, N. D., Niyogi, D., Rabin, S. S., Sloat, L., Wada, Y., Zappa, L., Chen, F., Cook, B. I., Kim, H., Lombardozzi, D., Polcher, J., Ryu, D., Santanello, J., Satoh, Y., Seneviratne, S., Singh, D., and Yokohata, T.: Irrigation in the Earth system, Nature Reviews Earth & Environment, 4, 435-453, 10.1038/s43017-023-00438-5, 2023.
McNairn, H., Champagne, C., Shang, J., Holmstrom, D., and Reichert, G.: Integration of optical and Synthetic Aperture Radar (SAR) imagery for delivering operational annual crop inventories, Int. J. Photogramm. Remote Sens., 64, 434-449,
670 10.1016/j.isprsjprs.2008.07.006, 2009.
Meier, J., Zabel, F., and Mauser, W.: A global approach to estimate irrigated areas – a comparison between different data and statistics, Hydrol. Earth Syst. Sci., 22, 1119-1133, 10.5194/hess-22-1119-2018, 2018.
Nabil, M., Zhang, M., Bofana, J., Wu, B., Stein, A., Dong, T., Zeng, H., and Shang, J.: Assessing factors impacting the spatial discrepancy of remote sensing based cropland products: A case study in Africa, Int. J. Appl. Earth Obs. Geoinf., 85, 102010,
675 2020.
Nagaraj, D., Proust, E., Todeschini, A., Rulli, M. C., and D'Odorico, P.: A new dataset of global irrigation areas from 2001 to 2015, Adv. Water Resour., 152, 103910, 10.1016/j.advwatres.2021.103910, 2021.
Pervez, M. S. and Brown, J. F.: Mapping Irrigated Lands at 250-m Scale by Merging MODIS Data and National Agricultural Statistics, Remote Sensing, 2, 2388-2412, 10.3390/rs2102388, 2010.
680 Potapov, P., Turubanova, S., Hansen, M. C., Tyukavina, A., Zalles, V., Khan, A., Song, X.-P., Pickens, A., Shen, Q., and Cortez, J.: Global maps of cropland extent and change show accelerated cropland expansion in the twenty-first century, Nature Food, 3, 19-28, 2022.

Puy, A., Borgonovo, E., Lo Piano, S., Levin, S. A., and Saltelli, A.: Irrigated areas drive irrigation water withdrawals, Nat Commun, 12, 4525, 10.1038/s41467-021-24508-8, 2021.

Puy, A., Sheikholeslami, R., Gupta, H. V., Hall, J. W., Lankford, B., Lo Piano, S., Meier, J., Pappenberger, F., Porporato, A., Vico, G., and Saltelli, A.: The delusive accuracy of global irrigation water withdrawal estimates, Nat Commun, 13, 3183, 10.1038/s41467-022-30731-8, 2022.

Salmon, J. M., Friedl, M. A., Frolking, S., Wisser, D., and Douglas, E. M.: Global rain-fed, irrigated, and paddy croplands: A new high resolution map derived from remote sensing, crop inventories and climate data, Int. J. Appl. Earth Obs. Geoinf., 38, 321-334, 10.1016/j.jag.2015.01.014, 2015.

Shahriar Pervez, M., Budde, M., and Rowland, J.: Mapping irrigated areas in Afghanistan over the past decade using MODIS NDVI, RSEnv, 149, 155-165, 10.1016/j.rse.2014.04.008, 2014.

Siebert, S., Henrich, V., Frenken, K., and Burke, J.: Update of the digital global map of irrigation areas to version 5, Rheinische Friedrich-Wilhelms-Universität, Bonn, Germany and Food and Agriculture Organization of the United Nations, Rome, Italy, 2013.

Siebert, S., Döll, P., Hoogeveen, J., Faures, J.-M., Frenken, K., and Feick, S.: Development and validation of the global map of irrigation areas, 2005.

Siebert, S., Kummu, M., Porkka, M., Döll, P., Ramankutty, N., and Scanlon, B. R.: A global data set of the extent of irrigated land from 1900 to 2005, HESS, 19, 1521-1545, 2015.

Teluguntla, P., Thenkabail, P., Oliphant, A., Gumma, M., Aneece, I., Foley, D., and McCormick, R.: Landsat-Derived Global Rainfed and Irrigated-Cropland Product 30 m V001 [dataset], https://doi.org/10.5067/Community/LGRIP/LGRIP30.001, 2023.

Thenkabail, P. S., Knox, J. W., Ozdogan, M., Gumma, M. K., Congalton, R. G., Wu, Z., Milesi, C., Finkral, A., Marshall, M., and Mariotto, I.: Assessing future risks to agricultural productivity, water resources and food security: How can remote sensing help?, PE&RS, Photogrammetric Engineering & Remote Sensing, 78, 773-782, 2012.

Thenkabail, P. S., Biradar, C. M., Noojipady, P., Dheeravath, V., Li, Y., Velpuri, M., Gumma, M., Gangalakunta, O. R. P., Turral, H., Cai, X., Vithanage, J., Schull, M. A., and Dutta, R.: Global irrigated area map (GIAM), derived from remote sensing, for the end of the last millennium, Int. J. Remote Sens., 30, 3679-3733, 10.1080/01431160802698919, 2009.

Tian, F., Wu, B., Zeng, H., Watmough, G. R., Zhang, M., and Li, Y.: Detecting the linkage between arable land use and poverty using machine learning methods at global perspective, Geography and Sustainability, 3, 7-20, 10.1016/j.geosus.2022.01.001, 2022.

Tian, F., Wu, B., Zeng, H., Zhang, M., Zhu, W., Yan, N., and Lu, Y.: GMIE: a global maximum irrigation extent and irrigation type dataset derived through irrigation performance during drought stress and machine learning method (V2), Harvard Dataverse [dataset], doi:10.7910/DVN/HKBAQQ, 2023a.

Tian, F., Wu, B., Zeng, H., Zhang, M., Hu, Y., Xie, Y., Wen, C., Wang, Z., Qin, X., Han, W., and Yang, H.: A Shape-attention Pivot-Net for Identifying Central Pivot Irrigation Systems from Satellite Images using a Cloud Computing Platform: An

application in the contiguous US, GIScience & Remote Sensing, 10.1080/15481603.2023.2165256, 2023b.

Waldner, F., De Abelleyra, D., Verón, S. R., Zhang, M., Wu, B., Plotnikov, D., Bartalev, S., Lavreniuk, M., Skakun, S., and Kussul, N.: Towards a set of agrosystem-specific cropland mapping methods to address the global cropland diversity, Int. J. Remote Sens., 37, 3196-3231, 2016.

Waller, P. and Yitayew, M.: Center Pivot Irrigation Systems, in: Irrigation and Drainage Engineering, edited by: Waller, P., and Yitayew, M., Springer International Publishing, Cham, 209-228, 10.1007/978-3-319-05699-9_12, 2016.

Wang, X., Muller, C., Elliot, J., Mueller, N. D., Ciais, P., Jagermeyr, J., Gerber, J., Dumas, P., Wang, C., Yang, H., Li, L., Deryng, D., Folberth, C., Liu, W., Makowski, D., Olin, S., Pugh, T. A. M., Reddy, A., Schmid, E., Jeong, S., Zhou, F., and Piao, S.: Global irrigation contribution to wheat and maize yield, Nat Commun, 12, 1235, 10.1038/s41467-021-21498-5, 2021.

Wriedt, G., Der Velde, M. V., Aloe, A., and Bouraoui, F.: A European irrigation map for spatially distributed agricultural modelling, Agricultural Water Management, 96, 771-789, 2009.

Wu, B., Tian, F., Zhang, M., Zeng, H., and Zeng, Y.: Cloud services with big data provide a solution for monitoring and tracking sustainable development goals, Geography and Sustainability, 1, 25-32, 10.1016/j.geosus.2020.03.006, 2020.

Wu, B., Fu, Z., Fu, B., Yan, C., Zeng, H., and Zhao, W.: Dynamics of land cover changes and driving forces in China's drylands since the 1970 s, Land Use Policy, 140, 107097, 10.1016/j.landusepol.2024.107097, 2024.

Wu, B., Tian, F., Zhang, M., Piao, S., Zeng, H., Zhu, W., Liu, J., Elnashar, A., and Lu, Y.: Quantifying global agricultural water appropriation with data derived from earth observations, Journal of Cleaner Production, 358, 131891, 10.1016/j.jclepro.2022.131891, 2022.

Wu, B., Gommes, R., Zhang, M., Zeng, H., Yan, N., Zou, W., Zheng, Y., Zhang, N., Chang, S., and Xing, Q.: Global Crop Monitoring: A Satellite-Based Hierarchical Approach, Remote Sensing, 7, 3907-3933, 2015.

Wu, B., Qian, J., Zeng, Y., Zhang, L., Yan, C., Wang, Z., Li, A., Ma, R., Yu, X., and Huang, J.: Land Cover Atlas of the People's Republic of China (1: 1 000 000), Science Bulletin, 65, 1125-1136, 2017.

Wu, B., Tian, F., Nabil, M., Bofana, J., Lu, Y., Elnashar, A., Beyene, A. N., Zhang, M., Zeng, H., and Zhu, W.: Mapping global maximum irrigation extent at 30m resolution using the irrigation performances under drought stress, Global Environmental Change, 79, 102652, 10.1016/j.gloenvcha.2023.102652, 2023a.

Wu, B., Zhang, M., Zeng, H., Tian, F., Potgieter, A. B., Qin, X., Yan, N., Chang, S., Zhao, Y., Dong, Q., Boken, V., Plotnikov, D., Guo, H., Wu, F., Zhao, H., Deronde, B., Tits, L., and Loupian, E.: Challenges and opportunities in remote sensing-based crop monitoring: a review, Natl Sci Rev, 10, nwac290, 10.1093/nsr/nwac290, 2023b.

Xiang, K., Ma, M., Liu, W., Dong, J., Zhu, X., and Yuan, W.: Mapping Irrigated Areas of Northeast China in Comparison to Natural Vegetation, Remote Sensing, 11, 825, 10.3390/rs11070825, 2019.

Xie, Y. and Lark, T. J.: Mapping annual irrigation from Landsat imagery and environmental variables across the conterminous United States, RSEnv, 260, 112445, 10.1016/j.rse.2021.112445, 2021.

Xie, Y., Gibbs, H. K., and Lark, T. J.: Landsat-based Irrigation Dataset (LANID): 30 m resolution maps of irrigation distribution,

frequency, and change for the US, 1997–2017, Earth System Science Data, 13, 5689-5710, 2021.

Xie, Y., Lark, T. J., Brown, J. F., and Gibbs, H. K.: Mapping irrigated cropland extent across the conterminous United States at 30 m resolution using a semi-automatic training approach on Google Earth Engine, Int. J. Photogramm. Remote Sens., 155, 136-149, 10.1016/j.isprsjprs.2019.07.005, 2019.

Yu, L., Wang, J., and Gong, P.: Improving 30 m global land-cover map FROM-GLC with time series MODIS and auxiliary data sets: a segmentation-based approach, Int. J. Remote Sens., 34, 5851-5867, 2013.

Zajac, Z., Gomez, O., Gelati, E., van der Velde, M., Bassu, S., Ceglar, A., Chukaliev, O., Panarello, L., Koeble, R., van den Berg, M., Niemeyer, S., and Fumagalli, D.: Estimation of spatial distribution of irrigated crop areas in Europe for large-scale modelling applications, Agr Water Manage, 266, 107527, 10.1016/j.agwat.2022.107527, 2022.

Zanaga, D., Van De Kerchove, R., Daems, D., De Keersmaecker, W., Brockmann, C., Kirches, G., Wevers, J., Cartus, O., Santoro, M., and Fritz, S.: ESA WorldCover 10 m 2021 v200, 2022.

Zhang, C., Dong, J., and Ge, Q.: Mapping 20 years of irrigated croplands in China using MODIS and statistics and existing irrigation products, Scientific Data, 9, 407, 2022a.

Zhang, C., Dong, J., and Ge, Q.: Mapping 20 years of irrigated croplands in China using MODIS and statistics and existing irrigation products, Sci Data, 9, 407, 10.1038/s41597-022-01522-z, 2022b.

Zhang, C., Dong, J., and Ge, Q.: IrriMap_CN: Annual irrigation maps across China in 2000–2019 based on satellite observations, environmental variables, and machine learning, RSEnv, 280, 113184, 10.1016/j.rse.2022.113184, 2022c.

Zhang, L., Zhang, K., Zhu, X., Chen, H., and Wang, W.: Integrating remote sensing, irrigation suitability and statistical data for irrigated cropland mapping over mainland China, JHyd, 613, 128413, 10.1016/j.jhydrol.2022.128413, 2022d.

Zhang, M., Wu, B., Zeng, H., He, G., Liu, C., Tao, S., Zhang, Q., Nabil, M., Tian, F., and Bofana, J.: GCI30: a global dataset of 30 m cropping intensity using multisource remote sensing imagery, Earth System Science Data, 13, 4799-4817, 2021a.

Zhang, X., Liu, L., Chen, X., Gao, Y., Xie, S., and Mi, J.: GLC_FCS30: Global land-cover product with fine classification system at 30 m using time-series Landsat imagery, Earth System Science Data, 13, 2753-2776, 2021b.

Zhu, X., Zhu, W., Zhang, J., and Pan, Y.: Mapping irrigated areas in China from remote sensing and statistical data, IEEE Journal of Selected Topics in Applied Earth Observations and Remote Sensing, 7, 4490-4504, 2014.

Zomer, R. J., Xu, J., and Trabucco, A.: Version 3 of the Global Aridity Index and Potential Evapotranspiration Database, Sci Data, 9, 409, 10.1038/s41597-022-01493-1, 2022.